NACA

RESEARCH MEMORANDUM

INVESTIGATION OF BLADE-ROW FLOW DISTRIBUTIONS IN AXIAL-FLOW-COMPRESSOR STAGE CONSISTING OF GUIDE VANES AND ROTOR-BLADE ROW

By John J. Mahoney, Paul D. Dugan, Raymond E. Budinger
and H. Fred Goelzer

Lewis Flight Propulsion Laboratory
Cleveland, Ohio

NATIONAL ADVISORY COMMITTEE
FOR AERONAUTICS

WASHINGTON
November 28, 1950

NATIONAL ADVISORY COMMITTEE FOR AERONAUTICS

RESEARCH MEMORANDUM

INVESTIGATION OF BLADE-ROW FLOW DISTRIBUTIONS IN AXIAL-FLOW-COMPRESSOR STAGE CONSISTING OF GUIDE VANES AND ROTOR-BLADE ROW

By John J. Mahoney, Paul D. Dugan

Raymond E. Budinger, and H. Fred Goelzer

SUMMARY

A 30-inch tip-diameter axial-flow compressor stage was designed and operated to investigate individual blade-row performance and interblade-row effects. The stage consisted of 40 sheet-metal inlet guide vanes, and 29 rotor blades with a constant NACA 65-(12)10 airfoil section. This stage had a hub-to-tip diameter ratio of 0.8 at the rotor inlet. Instrumentation was provided to study the flow leaving the guide vanes without the rotor. The rotor was installed and instrumentation was added to investigate over-all rotor performance, the effect of a rotating blade row on the flow leaving the guide vanes, the rotor-blade-element performance, and the flow conditions in the outer-wall boundary layer.

Over-all rotor-performance results at the design speed of 840 feet per second gave a peak adiabatic efficiency of 0.900 with a rotor total-pressure ratio of 1.287 at a corrected weight flow of approximately 52.40 pounds per second. For design angle of attack at the mean radius, corresponding to 56.20 pounds per second, the efficiency was 0.880 and the pressure ratio was 1.240. A maximum total-pressure ratio of 1.330 with an efficiency of 0.750 was reached at approximately 40.00 pounds per second.

Flow conditions at the guide-vane outlet without the rotor agreed closely with the design assumptions, except that the angles of flow near the hub and the tip were lower than design. With the rotor operating downstream of the guide vanes, the increase in angles leaving the guide vanes was explained on the basis of the difference in guide-vane-inlet Mach number between the investigations with and without the rotor. This explanation was limited to the mean region of the annulus in the high- and medium-flow ranges of rotor operation. Near the hub and the tip, however, the flow angles were

increased approximately 1.3° by the presence of the rotor. In the low-flow region above a value of 0.36 for the nondimensional rotor-blade-element loading parameter, the angles at which air left the guide vanes at the mean radius increased at the three speeds in comparison with angles calculated for the guide-vane runs without the rotor.

The design assumption of simple radial equilibrium at the guide-vane outlet was satisfied when the measured leaving angles were considered; but this assumption was invalid if the rotor was in operation.

In comparison with two-dimensional cascade data, the curves of rotor-blade turning angle plotted against angle of attack over the outer half of the annulus, in general, indicated higher turning and were parallel to the two-dimensional curves, although blade stall near the tip was evidenced at an angle of attack of 11°, which was lower than that obtained in the two-dimensional investigation. Near the hub, the measured turning-angle curves had a steeper slope than the two-dimensional curves with less turning at low angles of attack and more turning at the high-angle-of-attack end of the two-dimensional-cascade curve.

The condition of simple radial equilibrium based on the assumptions of constant energy addition and no radial entropy gradient was not satisfied at the rotor outlet for a weight flow corresponding to design angle of attack at the mean radius; the maximum discrepancy in axial velocity was 2 percent near the hub.

Boundary-layer studies showed that the outer-wall boundary-layer displacement thickness was less than 1.0 percent of the passage height at the guide-vane outlet under all conditions, and less than 1.5 percent of the passage height downstream of the rotor, before the rotor blade stalled at the tip. The displacement thickness at the rotor outlet rapidly increased after the rotor blade stalled.

INTRODUCTION

In order to predict accurately the performance of axial-flow compressors and to improve design procedures, experimental studies of the flow processes in individual blade rows and investigations of interblade-row effects are essential. Three-dimensional and secondary effects, such as boundary-layer development, radial and induced flows, and compressibility, result in discrepancies between the actual blade-row flow distributions and the optimum values prescribed

by present two-dimensional design procedures. These flow discrepancies produce losses in individual blade-row performance and lead to mismatching of succeeding blade rows.

The complete experimental evaluation of the flow through axial-flow compressors requires detailed measurements of radial- and axial-flow distributions across each blade row. This evaluation is an extremely complex problem because of size, space, and instrumentation requirements of such a program.

An approach to the problem was made at the NACA Lewis laboratory by investigating a 30-inch tip-diameter axial-flow-compressor stage, which provided sufficient space for the instrumentation required to permit a detailed analysis of blade-row flow distributions. This compressor was geometrically similar to the typical middle stage of a conventional multistage compressor and had a hub-to-tip diameter ratio of 0.8 at the rotor-blade inlet. The compressor stage consisted of a set of 40 circular-arc constant-thickness guide vanes, which imposed a wheel or solid-body-type rotation on the entering air, and 29 constant-chord NACA 65-(12)10 rotor blades, which added a vortex rotation to the air.

The interference effect of an adjacent blade row on the angle and velocity distributions at the guide-vane outlet was studied by investigating the flow leaving the guide vanes with and without the rotor installed. The compressor rotor was operated at corrected rotor-tip speeds of 504, 672, and 840 feet per second, which represented 60 percent, 80 percent, and design speed (840 ft/sec), respectively. The range of Reynolds number, based on blade chord, was 490,000 to 820,000 and the Mach number of the flow relative to the rotor blades varied from 0.36 to 0.70.

The over-all performance of the rotor is presented as plots of total-pressure ratio and adiabatic temperature-rise efficiency against corrected weight flow. The rotor-blade-element performance is compared with two-dimensional cascade results, and this analysis of blade-row performance is complemented by measurements of outer-wall boundary layer upstream and downstream of the rotor-blade row.

APPARATUS

Aerodynamic compressor design. - The radial distribution of flow for this design was based on a wheel-type rotation leaving the guide vanes and a vortex-type rotation added by the rotor with a symmetrical velocity diagram at the rotor hub (50-percent reaction). In

establishing the velocity-vector diagrams at all radii, the following design criterions were used:

(1) Constant tip diameter

(2) Hub-to-tip diameter ratio at rotor-blade inlet equal to 0.8

(3) Ratio of axial velocity at hub to tip speed at rotor inlet equal to 0.6 (approximate condition for maximum power input)

(4) Value of change in tangential component of velocity at hub through the rotor blades set by σC_L limitation of 0.99 (All symbols are defined in appendix A.)

(5) Relative inlet Mach number at rotor-blade tip equal to 0.7

(6) Constant total enthalpy from hub to tip and simple radial equilibrium of static pressures downstream of each blade row

(7) Absolute Mach number at hub at rotor-blade outlet equal to relative Mach number at hub entering rotor blades

(8) Hub taper determined by radial equilibrium and continuity requirements with an assumed adiabatic compression efficiency of 0.89.

Inlet guide vanes were fabricated from 1/8-inch thick sheet metal and had a circular-arc mean camber line with a constant radius of curvature from hub to tip (fig. 1(a)). The camber was varied to give the required prerotation to the air at each radius by adjusting the chord length. The guide vanes were designed for a wheel-type rotation with the axial-velocity distribution computed on the basis of simple radial equilibrium of static pressure. An NACA constant chord 65-(12)10 airfoil section was used for the rotor blades at all radii (fig. 1(b)). The blade-angle settings necessary to produce the design turning angles were determined from the following relation between turning angle and angle of attack (reference 1):

$$\Delta\beta' = K\,(\alpha-\alpha_0) \qquad (1)$$

where K is a function of the inlet-air angle and cascade solidity. The calculated radial variation of blade-angle setting was corrected by an approximate method to account for the change in axial velocity

across the blade caused by hub taper and to satisfy radial-equilibrium requirements. Pertinent design values at the measuring stations are presented in the following table (station locations and symbols refer to figs. 2 and 3):

Radial position	Radius ratio at station 1	Rotor solidity, σ	Air angle at guide-vane outlet, β_1 (deg)	Relative air angle, β'_1 (deg)	Turning angle, $\Delta\beta'_1$ (deg)	Angle of attack, α (deg)	Blade angle setting φ (deg)	Ratio of axial velocity to rotor-tip speed		Radius ratio at station 2
								Station 1	Station 2	
Tip	1.0000	0.8902	26.64	52.64	12.60	4.84	47.80	0.5521	0.5210	1.0000
a	.9817	.9067	26.01	51.88	13.55	5.94	45.94	.5571	.5312	.9827
b	.9442	.9428	24.76	50.29	15.41	8.36	41.93	.5670	.5512	.9480
c	.9051	.9835	23.49	48.62	17.39	10.85	37.77	.5767	.5713	.9120
d	.8642	1.0301	22.21	46.83	19.46	13.43	33.40	.5862	.5914	.8747
e	.8213	1.0838	20.90	44.92	21.66	16.09	28.83	.5956	.6118	.8360
Hub	.8000	1.1127	20.27	43.92	22.54	17.32	26.60	.6000	.6212	.8176

Mechanical compressor design. - A cross-sectional view of the compressor and the inlet bellmouth is shown in figure 2. The compressor had a constant tip diameter of 30.00 inches, and the stationary clearance between the rotor-blade tips and the compressor casing was 0.015 inch. There was a minimum axial distance of approximately 0.85 inch between the trailing edge of the guide vanes at the tip and the leading edge of the rotor blades at the same radial position. The inner wall of the bellmouth was smoothly tapered from a 50-inch diameter to a 30-inch diameter in an axial distance of 20 inches.

Compressor installation. - A schematic drawing of the compressor installation is presented in figure 4. Air was drawn in from the test cell through a valve, the principal function of which was to control the total pressure at the compressor inlet. The air then flowed through a submerged orifice located in a length of straight pipe, as recommended in reference 2. A depression tank, 90 inches in diameter and 178 inches long, was used to maintain the inlet dynamic pressure within the limits recommended in reference 3. In order to minimize flow deviations from the axial direction and to provide uniform air flow into the compressor, two 60-mesh 0.008 screens were placed in the depression tank. Angle and pressure surveys in the radial direction at several circumferential positions at the compressor inlet indicated that the flow distribution was uniform within the limits recommended in reference 3. The compressor-outlet collector was connected to the laboratory altitude

exhaust system by means of two ducts. Air-weight flow was controlled primarily by an outlet valve located in the exhaust system.

INSTRUMENTATION

In this investigation, the weight flow through the compressor was measured by a submerged thin-plate orifice with a 0.55-diameter ratio. This orifice was installed and instrumented according to the specifications given in reference 2. The compressor speed was measured with a chronometric-type tachometer. For the evaluation of over-all performance and individual blade-row flow details, extensive instrumentation was located at stations 0, 1, and 2, as shown in figures 2 and 4.

Station 0 was used to determine the compressor-inlet conditions and was instrumented in accordance with the recommendations of reference 3.

Station 1 was located approximately 1/6-rotor-blade chord length upstream of the leading edge of the rotor blades at the tip; the data taken at this station were used to evaluate both the guide-vane-outlet flow conditions and the rotor-inlet flow conditions. Three circumferential slots, each covering 12° and representing 4/3 of a passage between two adjacent guide vanes, were used to obtain circumferential surveys. The centers, or 0° positions, of these instrument slots were located 45° apart on the upper half of the casing with the middle slot straddling the vertical center line of the compressor.

Total pressures were obtained with a survey probe of the type shown in figure 5(a). A claw-type yaw tube (fig. 5(b)) was used for measuring flow angle, and a wedge-type static pressure survey probe (fig. 5(c)) completed the survey instrumentation. The total temperature was assumed to remain constant across the guide vanes. An average of the pressure measured by five wall static taps, equally spaced around the periphery of the compressor, was used to obtain the static pressure at the outer wall.

The survey instruments at station 2 (approximately 1/4-chord length downstream of the rotor) were similar to those at station 1 and were used to evaluate the rotor-outlet conditions, as well as the over-all rotor performance. These instruments were used for radial surveys only and were located around the periphery so that the measurements would be unaffected by the wakes of upstream instruments. Total-temperature measurements were taken with five rakes each containing five thermocouple probes (fig. 5(d)). These rakes

were equally spaced around the periphery, and the individual probes on each rake were radially located at the centers of five equal areas across the annulus. All five probes at the same radial position were so connected in series with five probes in the depression tank that a circumferential sum of five temperature rises across the rotor at each of the five radial positions could be recorded. The thermocouple rakes were set at 45° to the compressor axis, so that the flow angle at most operating conditions fell within the permissible yaw angle of the instrument, as determined by calibration. In addition to this instrumentation, four wall static taps were provided in the casing.

ACCURACY OF MEASUREMENT

All instruments used in this investigation were calibrated in a steady-flow tunnel over the same range of Mach numbers and Reynolds numbers encountered in the compressor investigation. Thermocouple calibrations indicated that the temperature-recovery coefficient increased in magnitude with increasing Mach number and was unaffected by yaw angles up to ±15°. Over most of the operating range for the rotor blades, the flow angle at station 2 was within the permissible yaw-angle range. Wedge-type static-pressure probes are subject to wall and stem effects in addition to Mach number effects. The correction curves for the wedge-static probes used in this investigation are illustrated by figure 6, where correction factor is plotted against Mach number for the various radial positions in the compressor. All instruments were frequently checked for oil and dirt accumulations, and check points periodically taken indicated consistent results. The effects of radial and unsteady flows were not evaluated in the instrument calibrations.

As an indication of the accuracy of the compressor instrumentation, the integrated weight flows upstream and downstream of the rotor were compared with the orifice-measured weight flow. At station 1, weight flows representing the high-, medium-, and low-flow ranges at each speed, were both radially and circumferentially integrated; they checked the orifice-measured weight flow within ±1.0 percent under all conditions.

At station 2, the discrepancy between integrated and orifice-measured weight flows varied from -2.0 to 7.0 percent for the range of operating conditions investigated. Although this discrepancy was not definitely related to any variation in weight flow, in general, the integrated weight flow was higher than the orifice-measured weight flow. For the high- and medium-flow ranges at all speeds, the discrepancy did not exceed ±2.0 percent. In the low-flow

range at all speeds, however, the discrepancy rapidly increased with decreasing weight flow. The increase in discrepancy in the low-weight-flow region is probably caused by an increase in the effect on the instrumentation of the fluctuating pressure field caused by the enlarged rotating blade wakes.

Some of the discrepancy between the integrated weight flows at stations 1 and 2, and the weight flow measured by the orifice may be charged to radial components of flow because the velocities calculated from the pressure and temperature measurements were assumed to have no radial component. The error introduced by this flow component is small over most of the flow range, however, because a flow angularity of 10° in the radial direction causes an approximate error of only 1.5 percent in the axial velocity component. Two other effects, which may contribute to the discrepancy between integrated and orifice-measured weight flow, are circumferential-flow variations and unsteady flow. No attempt was made to evaluate the effect of unsteady-flow conditions, but flow variations around the compressor circumference were measured by interchanging the instruments in the various circumferential positions and were found to be negligible.

Because of the calibration techniques employed and the correlation observed between the integrated and orifice-measured weight flows, except in the low-flow region at station 2, it is estimated that the accuracy of measurement over most of the flow range covered in this investigation is as follows:

Static pressure, percent of dynamic head	±2.0
Total pressure, percent of dynamic head	±1.0
Air angle, deg	±0.5
Inlet temperature, $^{\circ}F$	±0.5
Outlet temperature, $^{\circ}F$	±1.0
Compressor speed, percent of rpm	±0.25

PROCEDURE

Operational

Initial guide-vane-performance measurements were taken at a corrected weight flow of 47.1 pounds per second with the guide vanes installed in the test rig without the rotor. In order to determine the flow distribution leaving the guide vanes, measurements in the circumferential direction were taken at every degree within the 12°-range of the instrument slots for each of the 10 radial positions

(fig. 2). These measurements indicated that the (-4) circumferential position represented very closely the circumferential average of the flow conditions leaving the guide vanes at all radii. The survey instruments were interchanged in the three slots, in order to detect any large-scale flow variations around the compressor periphery as differentiated from circumferential-flow variations within a blade passage.

For final guide-vane, rotor-blade element, and over-all rotor-performance measurements, the compressor stage was investigated. The rotor was operated at corrected tip speeds of 504, 672, and 840 feet per second, corresponding to 60 percent, 80 percent, and design speed, respectively. At each speed a range of weight flow was investigated from a flow at which a pressure rise was no longer obtained at the rotor-blade tip to a flow at which stall occurred across most of the blade from the tip to the mean radius. The upper limit of weight flow could not be obtained at design speed because of high pressure losses in the exhaust system. Absolute pressure in the inlet depression tank was maintained at 25 inches of mercury for all speeds and weight flows.

The range of Reynolds number, based on blade chord, was 490,000 to 820,000 and the Mach number of the flow relative to the rotor blades varied from 0.36 to 0.70.

Over the entire weight-flow range for each speed investigated, instrument surveys were taken at station 1 at five radial positions, designated a, b, c, d, and e (fig. 2), with the instruments installed in one circumferential position (-4) (fig. 2). These five radial positions were the centers of five equal areas across the annulus. At three weight flows, representing the high-, medium-, and low weight-flow ranges, five additional radial positions; a', b', c', d', e' (fig. 2), across the annulus, and ten radial positions, spaced 0.050 inch apart beginning at the outer wall, were surveyed. Six additional circumferential positions (-6), (-2), (0), (2), (4), (6) (fig. 2) were surveyed at the same three representative weight flows at radial positions a, b, c, d, and e.

The procedure for the determination of the radial distribution of flow at station 2 was similar to that used at station 1.

Calculations

Rotor total-pressure ratio. - The total-pressure ratio across the rotor is taken as a mass-weighted average based on the isentropic

power input as integrated across the flow passage, and is obtained from mechanical integration of the following equation:

$$\left(\frac{P_2}{P_1}\right)_{av} = \left\{ \frac{\int_{r_{h,2}}^{r_{t,2}} \left[\left(\frac{P_2}{P_1}\right)^{\frac{\gamma-1}{\gamma}} - 1 \right] \rho_2 V_{z,2} r_2 \, dr}{\int_{r_{h,2}}^{r_{t,2}} \rho_2 V_{z,2} r_2 \, dr} + 1 \right\}^{\frac{\gamma}{\gamma-1}}$$

Adiabatic efficiency. - The adiabatic temperature-rise efficiency is defined by the equation

$$\eta_{ad} = \frac{H_{ad}}{H_T}$$

The adiabatic work input per pound of air H_{ad} is calculated from the equation:

$$H_{ad} = Jc_p T_0 \left[\left(\frac{P_2}{P_1}\right)_{av}^{\frac{\gamma-1}{\gamma}} - 1 \right]$$

The actual work input per pound of air H_T is determined from the mass-weighted average total-temperature rise across the compressor, and is evaluated by a mechanical integration of the following relation:

$$H_T = \frac{Jc_p \int_{r_{h,2}}^{r_{t,2}} (T_2 - T_0) \, \rho_2 V_{z,2} r_2 \, dr}{\int_{r_{h,2}}^{r_{t,2}} \rho_2 V_{z,2} r_2 \, dr}$$

Lift and drag. - Coefficients of lift and drag used in this investigation are based on the work input to the air and the equivalent velocity diagram (fig. 3).

$$C_L = \frac{2gJc_p(T_2 - T_0)}{\sigma V'_m U} - C_D \tan \beta'_m$$

$$C_D = \frac{2 \cos \beta'_m}{\sigma V'^2_m} gJc_p \left[(T_2 - T_0) - T_0 Y\right]$$

The derivation of these equations is presented in appendix B.

RESULTS AND DISCUSSION

Over-all Rotor Performance

The over-all performance of the rotor is presented in figure 7 as plots of total-pressure ratio and adiabatic efficiency against corrected weight flow. The weight flow corresponding to design angle of attack at the mean radius (10.85°) of the rotor blades is represented by the bar on each curve. Although an upper weight flow corresponding to no pressure-rise at the tip could not be obtained at design speed because of prohibitive losses in the exhaust system, the attainment of a range of weight flows up to 60.16 pounds per second was adequate for evaluation of performance at this speed. The design-flow conditions at design speed (840 ft/sec) indicate a rotor total-pressure ratio of 1.240 with an adiabatic efficiency of 0.880 at a corrected weight flow of 56.20 pounds per second. A maximum total-pressure ratio of 1.330 was obtained at a corrected weight flow of 40.00 pounds per second with an adiabatic efficiency of 0.750. For the peak efficiency of 0.900, the pressure ratio was 1.287, and the corrected weight flow was approximately 52.40 pounds per second. The peak efficiency increased to approximately 0.940 at 80 percent of design speed and 0.945 at 60 percent of design speed.

Guide-Vane Performance

Flow distribution at guide-vane outlet without rotor. - Flow angles leaving the guide vanes at five radial positions are plotted against circumferential position in figure 8. The blade-wake region, which was determined on the basis of total-pressure defect, is shown. Flow-angle measurements in the region of this blade wake are shown

as dashed lines because the pressure-balancing yaw tubes are inaccurate in this region where large total-pressure gradients exist. The circumferential variation in flow angle, exclusive of measurements in the region of the blade wake, decreases with decreasing radius from approximately 5.0° at radial position a to 1.4° at radial position e. This trend in flow-angle variation may be charged to the different rates of blade boundary-layer build-up on the pressure and suction surfaces and to the effect of the circulation gradient imposed by a solid-body-type rotation, in which the circulation at the blade tip is much greater than that at the blade hub. The magnitude of the circumferential variation, however, is probably affected by the location of the instrument measuring plane with respect to the guide-vane trailing edge. As shown in figure 2, station 1 is relatively close to the guide-vane trailing edge near the tip, where the circulation and the blade boundary-layer build-up are greatest. In comparison, near the hub sufficient axial distance exists between the guide-vane trailing edge and the measuring plane to permit some dissipation of the blade wake. Flow variations of the approximate magnitude shown on figure 8 are evidence of the necessity for surveying in the circumferential direction and determining an average value of flow conditions leaving the guide vanes at each radial position.

Inasmuch as angle measurements at circumferential position (-4) showed good agreement with the arithmetic circumferential average for most radial positions, the radial distribution of flow angle at position (-4) is compared with the design distribution on figure 9. Over most of the passage, the measured angles correlate the design values within the accuracy of instrument measurement. Near the hub and the tip, however, the angles decrease below the design value with a maximum discrepancy of 1.2° occurring near the tip. These discrepancies probably result from secondary flows associated with the wall boundary layers and the design circulation gradient.

The radial distribution of circumferentially averaged axial-velocity components at the guide-vane outlet is shown in figure 10 as axial-velocity ratio, that is, the ratio of the axial velocity at any radius to the axial velocity at the mean radius. In comparison with the design distribution, which is also shown on figure 10, the measured values are higher over most of the passage with a maximum discrepancy of 2 percent at radial position a. This discrepancy may be partly caused by the deviation from design of the measured leaving-angle distribution, which affects the simple

radial-equilibrium condition. In order to determine the distribution of axial velocity required for simple radial equilibrium with the measured flow-angle distribution, axial-velocity components were obtained by means of the radial equilibrium relation presented in reference 4:

$$\frac{\partial H_M}{\partial r} = T\frac{\partial s}{\partial r} + \frac{V_u}{r}\frac{\partial (rV_u)}{\partial r} + V_z\frac{\partial V_z}{\partial r} - V_z\frac{\partial Vr}{\partial z}$$

For simple-radial-equilibrium calculations, the radial-velocity term $V_z\frac{\partial Vr}{\partial z}$ and the entropy-loss terms $T\frac{\partial s}{\partial r}$ are neglected. All radial-equilibrium calculations reported herein are based on the resulting simplified equation

$$\frac{\partial H_M}{\partial r} = \frac{V_u}{r}\frac{\partial (rV_u)}{\partial r} + V_z\frac{\partial V_z}{\partial r} \qquad (2)$$

At station 1, $\partial H_M/\partial r = 0$ and the tangential-velocity component V_u is expressed in terms of the measured leaving angle and axial velocity. This calculated distribution is also plotted in figure 10. The measured values are generally lower than the calculated values over the inner half of the annulus and higher than the calculated values over the outer half of the annulus with a maximum discrepancy of approximately 0.7 percent at radial position e. The slight discrepancy between the measured and calculated values may be due to radial-flow components. These results indicate that the design assumption of simple radial equilibrium is valid and can be used to predict the radial gradient of velocity at the outlet of the guide vanes if the actual leaving-angle gradient over the entire passage can be more accurately prescribed by design procedures.

Flow distribution at guide-vane outlet with rotor installed. - When a rotor-blade row is operated a short distance downstream of the guide vanes, definite effects on the flow distribution at the guide-vane outlet are noted. A comparison of the circumferentially averaged outlet angles plotted against radius ratio for the investigation of the guide vanes without the rotor and for the investigation with the rotor-blade row in operation is presented in figure 11. The three curves for runs with the rotor represent weight flows near the design angle of attack at the rotor mean radius for each of the three rotor-tip speeds investigated. Inasmuch as the weight flows and, consequently, the inlet Mach numbers are different

for the four experimental conditions, and flow angles leaving the guide vanes increase slightly with increasing inlet Mach number, as indicated by reference 5; all data in this figure were corrected to the inlet Mach number corresponding to that for the investigation of the guide vanes without the rotor according to reference 5. At the mean radius, where three-dimensional effects are minimized, good agreement is obtained between the data with and without the rotor. Near the blade tip, however, the angles leaving the guide vanes are increased approximately 1.3° by the presence of the rotor, whereas from a radius ratio of approximately 0.86 to 0.90 the guide-vane leaving angles are decreased slightly by the rotor. Below a radius ratio of 0.86, the leaving angles are again increased above the value for the investigation of the guide vanes without the rotor with a maximum discrepancy of 1.3° occurring near the hub. In general, over most of the annulus, the Mach number correction is adequate, within the limits of accuracy of angle measurement, to account for the discrepancies between the curves. The large variations near the hub and the tip, however, probably result from a combination of rotor-blade effects, including viscous drag associated with the rotor, the change in the guide-vane circulation due to unknown induced effects of the rotor, and the change in axial-velocity ratio across the guide vanes with rotor speed.

Flow angles leaving the guide vanes at the mean radius for the three corrected tip speeds are plotted against corrected weight flow in figure 12. Because the investigation of the guide vanes without the rotor was conducted at only one weight flow (47.1 lb/sec), the variation of flow angle with weight flow and, consequently inlet Mach number for this investigation was calculated by means of results presented in reference 5. This calculated curve is also shown in figure 12. Over the medium and high-flow regions of the weight-flow range for each speed, the Mach number effect seems adequate within the limits of experimental accuracy of measurement to explain the trend of the curves; but this effect is insufficient to account for the deviation between the leaving angles at each speed and the calculated guide-vane leaving angles over the low-flow range of the three curves. Although the reasons for this discrepancy in the low-flow region were not fully understood, an insight into the variation was obtained by plotting guide-vane leaving angles against a rotor-blade-element loading parameter. Flow angles leaving the guide vanes at the mean radius for the three corrected tip speeds are plotted in figure 13 against a nondimensional rotor-blade-element-loading parameter H/U_t^2 where H is defined as the total-enthalpy addition at the mean radius and equals $gJc_p(T_2 - T_0)$. In order to eliminate

the Mach number effects, these curves have been corrected to a guide-vane-inlet Mach number corresponding to that for the investigation of the guide vanes without the rotor. Inasmuch as the three curves begin to increase at approximately the same value $\left(H/U_t^2 = 0.36\right)$, it seems indicative that the rotor-blade-element loading is the principal factor causing deviation at low weight flows. Similar trends were observed at radial positions near the hub and the tip.

The radial distribution of average axial velocity at station 1 for a weight flow approximating the mean-radius design angle of attack at design speed is plotted on figure 14 as axial-velocity ratios determined from measurements. Axial-velocity ratios calculated from the simple equilibrium relation (equation (2)), in which the tangential velocity was expressed in terms of the axial velocity and the guide-vane leaving angles measured at design rotor speed, are also shown. In comparison, the measured values are higher than the calculated values over the inner half of the passage and lower than the calculated values over the outer half. The trend is the reverse of that observed in figure 10, and indicates that the streamlines at station 1 have been radially displaced inward toward the hub by the rotating rotor. The magnitude of this radial displacement is too great, however, to obtain simple radial equilibrium; consequently, the design assumption of simple radial equilibrium at the guide-vane outlet is invalid when the rotor is operating a short distance downstream of the guide vanes. This failure to satisfy the design assumption may be explained on the basis of results presented in reference 4, which shows that the radial-velocity term $V_z \frac{\partial Vr}{\partial z}$ should be incorporated in equation (2) to account for the presence of radial motion in blade rows with finite aspect ratios.

Rotor-Blade-Element Performance

An analysis of the rotor-blade-element performance requires a detailed knowledge of the relative angles and flow velocities at the rotor-blade-row inlet and of the variation of rotor-blade loading with these relative entering flow conditions.

Flow distribution entering rotor. - The average flow conditions entering the rotor (station 1) for four weight flows at design speed are presented in figure 15 as plots of relative air-inlet angle and relative inlet Mach number against radius ratio. Design values from hub to tip are also presented for comparison. The experimental air-inlet angles at all weight flows have a greater slope than the design

curve. At the weight flow for design angle of attack at the mean radius, the air-inlet angles are 0.7° lower than design near the hub and 2.0° higher than design at radial position a, which is near the blade tip. These deviations in air-inlet angle represent equal discrepancies in blade angle of attack and result from the induced-velocity effects on the flow distribution leaving the guide vanes and from the failure to achieve simple radial equilibrium of static pressure, as assumed in the design procedure. In the tip region, the experimental angles at all weight flows indicate a sharp rise due to the decrease in axial velocity in the outer-wall boundary layer. The Mach number curves exhibit the same general profile for the four weight flows. At the weight flow for design angle of attack at the mean radius, the experimental Mach number curve correlates the design curve near the hub, but is slightly lower than design over the outer half of the annulus with a maximum discrepancy of approximately 3 percent.

Variation of turning angle with angle of attack. - Rotor-blade performance is presented in figure 16 as plots of the relative turning angle across the rotor against angle of attack for the five radial positions at design speed. A range of angles of attack was obtained by varying the weight flow, which also varies the air-inlet angles, inasmuch as the rotor-blade-angle settings are fixed. The effect of air-inlet angle on turning angle is therefore included in this figure. Effects of axial-velocity variations across the blade chord are present in the curve based on the true velocity diagram (fig. 3). In order to compensate for this variable axial velocity, an equivalent constant axial-velocity diagram (fig. 3) was used, and these results are also presented on figure 16. This equivalent-diagram method is recommended in reference 6 to obtain a more exact basis of comparison between rotating-cascade results and constant axial-velocity two-dimensional cascade data.

The two-dimensional cascade curves on figure 16 were obtained by interpolation of the 65-(12)10 blade-section two-dimensional results (references 6, 7, and unpublished data) for solidities and air-inlet angles as determined in the compressor investigation. These curves were then empirically adjusted according to unpublished data to compensate for the difference in Mach number between stationary cascade and rotor-blade-row data. Inasmuch as two-dimensional-cascade results are only available for air-inlet angles below 60° and for small ranges of angle of attack, the curves are limited to a comparatively narrow range of angle of attack. The design values of turning angle obtained from equation (1) are shown in figure 16 for comparison. This equation and the interpolated cascade data give comparable values of turning angle in the region of the rotor-blade tip; but the equation gives values approximately 1.5° low at the hub section.

Comparison of the two experimental curves, based on the true- and equivalent-velocity diagram, shows correlation within 1° over the range of angle of attack corresponding to the range of values available from interpolated two-dimensional data for radial positions from b to e. This correlation is obtained because of small axial-velocity increases (maximum 10 percent) across the rotor blades. At radial position a, however, a decided discrepancy occurs between the two experimental curves as the angle of attack is increased above 11°. In the range of angle of attack above 11°, as much as a 50-percent reduction in axial velocity occurs across the rotor blades. The decrease in turning angle above an angle of attack of 11° on radial position a for the true-velocity-diagram curve indicates that blade stall occurs at a lower angle of attack for the rotating cascade than for the two-dimensional cascade. Within the range of interpolated two-dimensional-cascade results, the experimental rotor-blade-turning-angle curves are, in general, very nearly parallel to the two-dimensional-cascade curves except in the region of the hub. For the three radial positions from the tip to the mean radius, the experimental curves, in general, indicate greater turning of the air over the entire range of angle of attack than that predicted by the interpolated cascade data with a maximum discrepancy of approximately 1.6° at radial position a. At radial positions d and e, the rotating-cascade curves have a steeper slope than the interpolated two-dimensional curves, indicating less turning of the air at low angles of attack on the rotor and more turning of the air in the high-angle-of-attack region of the two-dimensional curve.

This general trend of high turning near the tip and low turning near the hub may be accounted for by unknown induced effects associated with the outer-wall boundary layer and the radial gradient of rotor-blade circulation. Another factor that influences the trend of the experimental turning-angle curves is radial flow or centrifuging of the blade boundary layers from hub to tip, as explained in reference 8. This radial motion of the blade boundary layers in a rotating cascade induces blade stall near the tip at a lower angle of attack than that obtained by stationary-cascade results; whereas, near the hub, this radial flow of the blade boundary-layer delays separation. Viscous drag associated with the rotating rotor hub will act to increase the turning angles near the hub, but the magnitude of this effect on the experimental turning angles at radial position e may be negligible.

Blade-element lift and drag forces. - Two useful parameters of rotor-blade loading and performance are presented in figure 17 as plots of nondimensional lift and drag coefficients for radial position a, c, and e against corrected weight flow at design speed. The

lift-coefficient curves for the three blade sections increase with decreasing weight flow and have a similar slope over the weight-flow range from 60.2 pounds per second to approximately 52.4 pounds per second. Below a weight flow of 52.4 pounds per second, the lift curve for radial position a indicates a stall condition, which was previously noted in the turning-angle plots of figure 16. The stall condition is accompanied by an increase in drag coefficient below a corrected weight flow of 52.4 pounds per second, which corresponds to an angle of attack of 11° for radial position a. Inasmuch as the drag curve for radial position c begins to increase rapidly below a corrected weight flow of approximately 48 pounds per second and the lift curve for this blade section indicates stall below 45 pounds per second, whereas the drag curve for radial position e remains relatively constant over most of the weight-flow range investigated, the stall condition has evidently progressed from the tip only as far as the mean region of the blade. Above a corrected weight flow of 48.0 pounds per second, the drag coefficient at the mean radius is less than that at the other two sections because the effects of wall boundary layers, blade-tip clearance, and hub taper are a minimum in this region of the blade.

This minimum-drag condition at the mean radius is reflected by the plot of lift-drag ratio against corrected weight flow and equivalent angle of attack in figure 18, where the highest lift-drag ratio, or blade-element efficiency, for the tip, mean, and hub radii occurs at radial position c. Values for this figure were determined from the faired curves of lift and drag coefficient shown in figure 17. In comparision with the hub section, however, the most efficient, or optimum, operating range of the mean section and of the tip section is restricted to a narrow weight-flow range. The stall condition, which progresses from tip to mean radius with decreasing weight flow, reduces the most efficient operating range of the blade sections affected. Maximum lift-drag ratios for radial positions a and c are obtained near the peak-efficiency weight flow of 52.4 pounds per second; but, at this weight flow, the maximum lift-drag ratio for radial position e was not reached.

These results indicate that the blade sections are not matched with regard to the most efficient operating range for all sections; however, although radial flows will affect the magnitude of the lift and drag coefficients, the fundamental concept of two-dimensional lift and drag seems applicable to single-stage-compressor design procedures for obtaining an indication of the most efficient operating point for a blade cascade.

Blade camber and peak efficiency. - At the weight flow of 56.2 pounds per second corresponding to design angle of attack at the mean radius, the three blade sections investigated were operating below their maximum values of lift-drag ratio (fig. 18). The blade sections were all operating at angles of attack lower than those required for peak blade-element efficiency. The reason for the deviation between the design point and the points of peak lift-drag ratio is explained on the basis of the results given in references 6 and 7, which indicate that the blade camber used was somewhat higher than that required to obtain the design turning angles at peak blade-element efficiency. Regardless of camber, however, some discrepancy will exist between the design angle of attack based on references 6 and 7 and the angle of attack for peak lift-drag ratio, because by the method used in references 6 and 7 the optimum angle of attack is selected on the basis of the flattest pressure distribution around the blade, which occurs at a lower angle of attack than that for peak lift-drag ratio over the range of Mach numbers covered in this investigation. The unequal deviations of the angle of attack for maximum lift-drag ratio from the design angle of attack at the three blade sections is principally attributed to the use of a constant camber section along the entire blade length. A variable camber blade might permit a more efficient matching of all blade sections and an increase in the maximum over-all efficiency.

Flow distribution at rotor outlet. - Flow angles leaving the rotor at four corrected weight flows at design speed are plotted against radius ratio in figure 19. The design radial distribution of flow angle is also presented in figure 19. For the weight flow representing design angle of attack at the mean radius, the experimental angles correlate the design values within the accuracy of angle measurement, except near the hub and the tip. The measured angles at radial position a and e are 1.3° and 1.5° higher than the design values, respectively. From radial position a to the outer casing, the actual flow angles rapidly increase in comparison to the design distribution. This sharp rise in flow angle is primarily caused by the decrease in axial velocity in the outer-wall boundary layer with the added effect of the high whirl velocity of the centrifuged-blade boundary layer. Flow-angle curves for the other three weight flows in figure 19 exhibit a trend similar to that observed for the design flow condition.

The radial distribution of measured axial-velocity components at the rotor outlet for a corrected weight flow approximating design angle of attack at design speed is shown in figure 20 as the ratio of the axial velocity at any radius to the axial velocity at the mean radius. Axial-velocity components, calculated by means of the simple radial-equilibrium equation (equation (2)) in which

$\partial H_M/\partial r$ was assumed equal to zero and the tangential-velocity component V_u was expressed in terms of the axial velocity and the absolute angle measured at design speed, are also plotted as velocity ratios on figure 20. The measured values of the axial-velocity ratio are, in general, higher over the inner half of the annulus and lower over the outer half with a maximum discrepancy of approximately 2 percent near the hub. These results, in comparison with radial-equilibrium calculations at station 1 (fig. 14), indicate that the streamlines are displaced radially inward through the rotor; the design assumption of simple radial equilibrium at the outlet of the rotor blade is invalid. Invalidation of the design assumption may result from oscillatory radial motion, entropy losses, and radial-energy variations.

The radial variation of energy addition across the rotor is plotted in figure 21 for four weight flows at design speed, and the design variation is shown for the purpose of comparison. Across most of the annulus, the energy addition is essentially constant for all weight flows. At the weight flow representing design angle of attack at the mean radius, the experimental values of energy addition correlate the design values within 4 percent in the radius-ratio range from 0.84 to 0.96. From a radius ratio of 0.96 to the tip, however, the curve of measured energy addition continuously increases from 4 percent to approximately 19 percent above the design distribution. This rise in energy addition near the tip is indicated in all the experimental curves and reflects the influence of the high blade loading in the casing boundary layer in conjunction with the high whirl component of the centrifuged-blade boundary layer. The most nearly constant radial-energy addition is obtained at a weight flow of 52.40 pounds per second, which represents peak over-all efficiency. In general, these curves indicate that a reasonably constant energy addition can be anticipated over a wide range of weight flows with this type of design; the design assumption of constant total enthalpy at the exit of the rotor $(\partial H_M/\partial r)$ is approximately correct across most of the passage.

Boundary Layer

Outer-wall boundary-layer investigations were conducted in order that some of the effects of boundary layer could be accounted for in axial-flow-compressor design procedures. From the outer-wall boundary-layer radial surveys at stations 1 and 2, the displacement thickness t^* was determined by a mechanical integration of the following general equation of the boundary-layer weight flow in an annular passage:

$$\int_{r_t-t}^{r_t} \rho_n v_{z,n} r \, dr - \int_{r_t-t}^{r_t} \rho V_z r \, dr = \int_{r_t-t^*}^{r_t} \rho_n v_{z,n} r \, dr$$

where n refers to extrapolated main-channel or free-stream conditions. The actual boundary-layer thickness t was determined from plots of the measured weight-flow term $\rho V_z r \, dr$ as the distance from the outer wall to a point where the curve of weight-flow distribution across the passage began to change slope rapidly. The slope of the weight-flow-distribution curve in the main channel was then extended from this point to the outer wall to depict the weight-flow distribution that would probably be expected with a nonviscous fluid. A weight-flow loss, which is chargeable to the boundary layer, is represented by the area between the extrapolated weight-flow distribution curve for a nonviscous fluid flow $\rho_n v_{z,n} r \, dr$ and the measured weight-flow-distribution curve in the boundary layer $\rho V_z r \, dr$. By definition, if this weight-flow loss were present in a nonviscous fluid flow, the effect would be similar to a reduction in the physical channel height by t^*, the displacement thickness.

Inasmuch as no measurements were taken in the boundary layer upstream of the guide vanes, the change in boundary-layer thickness and free-stream Reynolds number across the guide vanes could not be evaulated; but the effect of changes in the main stream flow on the boundary layer at one station downstream of the guide vanes was determined. Displacement thickness at station 1 is plotted against corrected weight flow for the three corrected tip speeds in figure 22. The value of t^* increases with decreasing weight flow from a minimum of 0.6 percent of the 0.250-foot passage height to a maximum of 1.0 percent of the passage height. The values of t^* downstream of the rotor are plotted against corrected weight flow for the three corrected tip speeds on figure 23. These curves are partly dashed because the absolute magnitude of the values in this region are unknown. Reynolds number effects may partly account for the trend of the curves in the solid region, but other factors including Mach number effects, changes in velocity across the blade rows, and rotor-blade loading probably contribute to the general trend of the displacement-thickness curves at both measuring stations. The influence of rotor-blade loading on the displacement thickness downstream of the rotor is also illustrated in figure 23 where t^* for the three corrected tip speeds is plotted against a nondimensional rotor-blade loading parameter gH_T/U_t^2, which represents an average of the total enthalpy

addition from hub to tip rather than a blade-element enthalpy addition, as previously used. The displacement thickness increases slightly with increasing blade-loading parameter for values from approximately 0.205 to 0.360. Above a value of 0.360, the displacement thickness rapidly increases with small changes in the blade-loading parameter. This sharp change in the slope of the displacement curve at 0.360 corresponds to an angle of attack of 11° on the tip radial position a section of the rotor blade. As shown on figure 16, this angle of attack of 11° indicates the inception of stall near the blade tip. After tip stall has occurred, the centrifuged-blade boundary layer, which has separated from the blade, combines with the casing boundary layer to produce a rapidly increasing displacement thickness. Before tip stall, however, less than 1.5 percent of the 0.229-foot passage height at the rotor outlet, which has a stationary tip clearance of 0.015 inch, is subjected to the outer-wall boundary-layer displacement thickness.

SUMMARY OF RESULTS

The following results were obtained from the investigation of a 30-inch axial-flow compressor stage, consisting of guide vanes and constant-camber rotor blades, which was designed to permit a detailed study of the complex flow processes in individual blade rows and of interblade row effects:

1. At design speed, a peak adiabatic efficiency across the rotor of 0.900 was obtained at a corrected weight flow of approximately 52.40 pounds per second and an over-all rotor total-pressure ratio of 1.287. For a corrected weight flow of 56.20 pounds per second, which represents design angle of attack at the mean radius, the adiabatic temperature-rise efficiency was 0.880 with a total-pressure ratio of 1.240. The maximum total-pressure ratio of 1.330 was obtained at a corrected weight flow of approximately 40.00 pounds per second with an efficiency of 0.750.

2. The flow angles at the guide-vane outlet without the rotor closely agreed with the design values across most of the annulus, but in the region of the hub and the tip the measured angles were lower than design with a maximum discrepancy of 1.2° near the tip. Furthermore, the design assumption of simple radial equilibrium was essentially satisfied at the outlet of the guide vanes without the rotor, when the measured variation of angles leaving the guide vanes was taken into account.

3. Over the medium and high weight-flow ranges investigated at each rotor-tip speed, the observed increase in guide-vane leaving

angle over the values obtained without the rotor at the mean radius was explained on the basis of the difference in the guide-vane inlet Mach number at which the runs with and without the rotor were conducted. Near the blade hub and tip, the inlet Mach number correction was inadequate to account for the approximate 1.3° increase in guide-vane leaving angle in the presence of the rotating blade row. In the low-weight-flow range above a value of 0.36 for a nondimensional rotor-blade-element loading parameter at the three rotor tip speeds, the guide-vane leaving angles at the mean radius increased in comparison with the values calculated for the guide vanes without the rotor. With the rotor operating a short distance downstream of the guide vanes, the design assumption of simple radial equilibrium in conjunction with the measured angles at the guide-vane outlet was invalid.

4. Within the range of interpolated two-dimensional cascade data, the measured variations of turning angle with angle of attack at the three outer radial positions across the rotor blades were, in general, parallel to the two-dimensional curves and indicated higher turning angles than those predicted by the two-dimensional data with a maximum discrepancy of 1.6° at the radial position near the tip. On the basis of the true-velocity diagram, the measured turning-angle curve at this radial position indicated that the blade stalled near the tip at an angle of attack of 11°, which was lower than that obtained in the two-dimensional investigation. This tip-stall condition at an angle of attack of 11° corresponded to a nondimensional rotor-blade loading parameter of 0.36. The rotating-cascade curves at the two radial positions near the hub had a steeper slope than the two-dimensional curves and showed less turning of the air at low angles of attack and more turning in the high angle of attack region of the interpolated two-dimensional curves.

5. Calculations of blade lift-drag ratio indicated that at the weight flow for peak over-all efficiency the blade sections near the tip and the mean, but not the hub, were operating close to their values for maximum lift-drag ratio. At the weight flow for design angle of attack at the mean radius, all three blade sections were operating below the maximum lift-drag ratio. The deviation of angle of attack for peak lift-drag ratio from the design angle of attack was not equal for the three blade sections.

6. The design assumption of simple radial equilibrium with constant energy addition and no radial entropy gradient in conjunction with measured angles at the outlet of the rotor was invalid at a weight flow near the design-angle-of-attack condition for the mean radius. The maximum discrepancy in axial velocity amounted to 2 percent near the hub.

7. Investigation of the outer-wall boundary layer revealed that the displacement thickness was less than 1.0 percent of the passage height at the guide-vane outlet over the entire range of operating conditions and less than 1.5 percent of the passage height at the rotor outlet, except in the high rotor-blade-loading range where tip stall occurred. After tip stall occurred, the outer-wall boundary-layer displacement thickness at the rotor exit increased very rapidly.

Lewis Flight Propulsion Laboratory,
National Advisory Committee for Aeronautics,
Cleveland, Ohio.

APPENDIX A

Symbols

The following symbols are used in this report:

C_D	drag coefficient
C_L	lift coefficient
C_L/C_D	lift-drag ratio
c	blade chord
c_p	specific heat at constant pressure, 0.243 Btu/lb-$^\circ$F
c_v	specific heat at constant volume, 0.174 Btu/lb-$^\circ$F
D	blade-element drag force, lb/ft
F	resultant force on blade element, lb/ft
g	standard acceleration due to gravity, 32.174 ft/sec^2
H	actual work input per slug at mean radius, ft-lb/slug
H_{ad}	adiabatic work input per pound of air, ft-lb/lb
H_M	total enthalpy per slug of air, ft-lb/slug
H_T	actual work input per pound calculated from total-temperature rise, ft-lb/lb
J	mechanical equivalent of heat, 778.26 ft-lb/Btu
K	constant in turning-angle relation
L	blade-element lift force, lb/ft
M	absolute Mach number of air
M'	relative inlet Mach number, ratio of relative inlet velocity to local velocity of sound
P	absolute total pressure, lb/sq ft

p	absolute static pressure, lb/sq ft
p_i	indicated static pressure, lb/sq ft
r	radius to blade element, ft
s	blade spacing, ft
T	total temperature, $^{\circ}R$
t	casing boundary-layer thickness, ft
t^*	casing boundary-layer displacement thickness, ft
U	velocity of blade at any radius r, ft/sec
V	absolute air velocity, ft/sec
V'	air velocity relative to rotor, ft/sec
v'	extrapolated free-stream velocity, ft/sec
W	weight flow, lb/sec
$\frac{W\sqrt{\theta}}{\delta}$	weight flow corrected to NACA standard sea-level conditions, lb/sec
Y	$(P_2/P_1)^{\frac{\gamma-1}{\gamma}} - 1$
Z	axial distance, ft
α	angle of attack, deg
α_0	angle of attack at zero lift, deg
β	flow angle or absolute air angle, angle between compressor axis and absolute air velocity, deg
β'	relative flow angle or relative air angle (stagger), angle between compressor axis and air velocity relative to rotor, deg
γ	ratio of specific heats, c_p/c_v, 1.3947 for normal air

$\Delta\beta'$ turning angle, angle between inlet and outlet relative air velocities, deg

$\Delta V'$ change in relative velocity across rotor

δ ratio of inlet total pressure to standard sea-level pressure

η_{ad} adiabatic efficiency of compressor

θ ratio of inlet total temperature to standard sea-level temperature

ρ density, slugs/cu ft

σ blade-element solidity, ratio of chord length to circumferential distance between adjacent blades, c/s

φ blade-angle setting, angle between compressor axis and blade chord, deg

Subscripts:

0 inlet depression tank

1 downstream of guide vanes

2 downstream of rotor

av average

e equivalent velocity vectors based on constant axial-velocity diagram

h hub

m mean of inlet and outlet conditions

r radial

$\bar{r}$ mean radius

t tip

z axial

u tangential

APPENDIX B

DERIVATION OF EQUATIONS

Lift and drag forces on the rotor blades at all radial positions were assumed to act normal and parallel, respectively, to the vector mean of the inlet and outlet velocities, as shown in figure 3. These forces are expressed in the following form consistent with isolated airfoil practice:

$$L = \frac{1}{2} C_L \rho_m V'^2_m c \tag{A1}$$

$$D = \frac{1}{2} C_D \rho_m V'^2_m c \tag{A2}$$

The tangential force F_u applied to the blades by virtue of their rotation in the air is composed of components of the lift and drag forces

$$F_u = L_u + D_u \tag{A3}$$

where $L_u = L \cos \beta'_m$, and $D_u = D \sin \beta'_m$. (fig. 3). Substitution of equations (A1) and (A2) in (A3) yields

$$F_u = \frac{1}{2} C_L \rho_m V'^2_m c \cos \beta'_m + \frac{1}{2} C_D \rho_m V'^2_m c \sin \beta'_m \tag{A4}$$

The tangential force F_u is evaluated from the rate of change of momentum in the tangential direction. Thus

$$F_u = \rho_m V'_m \cos \beta'_m s \, \Delta V'_u \tag{A5}$$

and by combining equations (A4) and (A5)

$$C_L = \frac{2\Delta V'_u}{\sigma V'_m} - C_D \tan \beta'_m \tag{A6}$$

Inasmuch as the work input per unit mass of air may be expressed in terms of the change in moment of momentum across the rotor, $U\Delta V'_u$ or in terms of the total-temperature rise $gJc_p(T_2-T_0)$ the change in

relative tangential velocity $\Delta V'_u$ may be equated to the temperature rise as follows, when radial deflections are neglected:

$$\Delta V'_u = \frac{gJc_p(T_2-T_0)}{U} \tag{A7}$$

This substitution was made because the determination of temperature rise was considered more accurate than the calculation of $\Delta V'_u$. By substituting equation (A7) in equation (A6)

$$C_L = \frac{2gJc_p(T_2-T_0)}{\sigma V'_m U} - C_D \tan \beta'_m \tag{A8}$$

The determination of the drag coefficient C_D is based on the assumption that the frictional energy expended can be represented by the product of drag force multiplied by mean velocity. From a power consideration, the total-energy addition must equal the useful energy input plus the energy expended to overcome friction, or mathematically

$$gJc_p(T_2-T_0)\rho_m V'_m \cos \beta'_m s =$$

$$gJc_p T_0 Y \rho_m V'_m \cos \beta'_m s + \frac{1}{2} C_D \rho_m V'^3_m c$$

Therefore

$$C_D = \frac{2 \cos \beta'_m}{\sigma V'^2_m} gJc_p \left[(T_2-T_0) - T_0 Y\right] \tag{A9}$$

REFERENCES

1. Kantrowitz, Arthur, and Daum, Fred L.: Preliminary Experimental Investigation of Airfoils in Cascade. NACA RB, July 1942.

2. Anon.: Flow Measurement 1940. A.S.M.E. Power Test Codes (Instruments and Apparatus Sec.), pub. by A.S.M.E. (New York), 1940.

3. NACA Subcommittee on Compressors: Standard Procedures for Rating and Testing Multistage Axial-Flow Compressors. NACA TN 1138, 1946.

4. Wu, Chung-Hua, and Wolfenstein, Lincoln: Application of Radial-Equilibrium Condition to Axial-Flow Compressor and Turbine Design. NACA Rep. 955, 1950. (Formerly NACA TN 1795.)

5. Lieblein, Seymour, and Sandercock, Donald M.: Compressibility Correction for Turning Angles of Axial-Flow Inlet Guide Vanes. NACA TN 2215, 1950

6. Bogdonoff, Seymour M., and Bogdonoff, Harriet E.: Blade Design Data for Axial-Flow Fans and Compressors. NACA ACR L5F07a, 1945.

7. Bogdonoff, Seymour M., and Hess, Eugene E.: Axial-Flow Fan and Compressor Blade Design Data at 52.5° Stagger and Further Verification of Cascade Data by Rotor Tests. NACA TN 1271, 1947.

8. Weske, John R.: An Investigation of the Aerodynamic Characteristics of a Rotating Axial-Flow Blade Grid. NACA TN 1128, 1947.

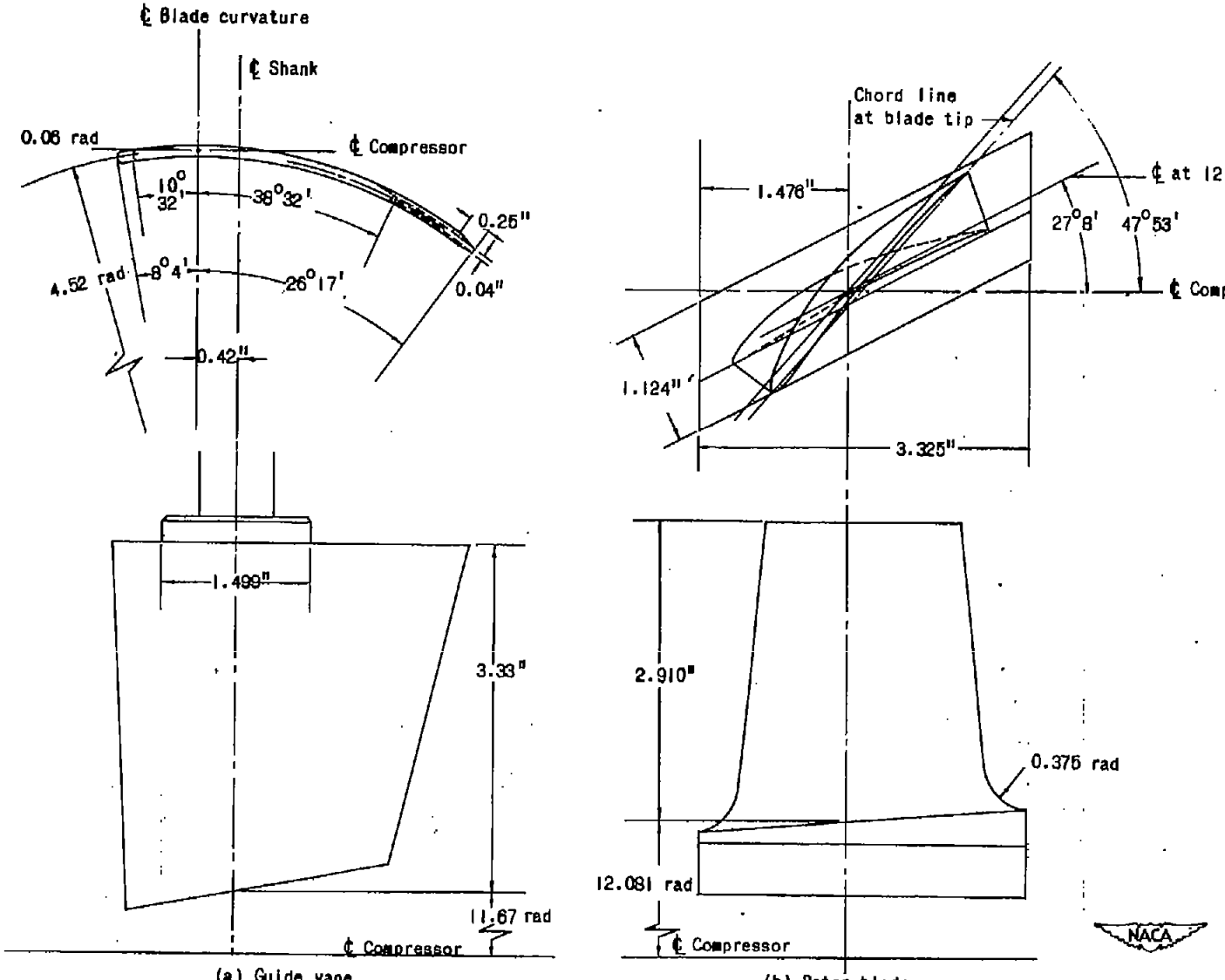

(a) Guide vane.

(b) Rotor blade.

Figure 1. - Compressor-blade drawings.

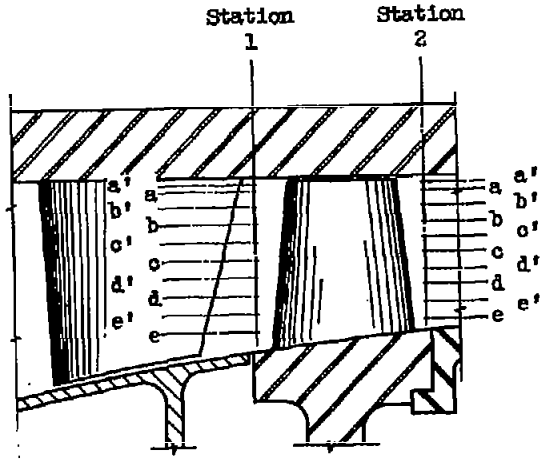

Detail B

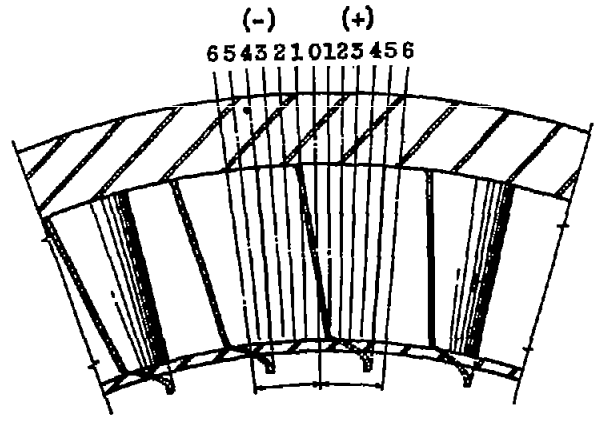

Section A-A

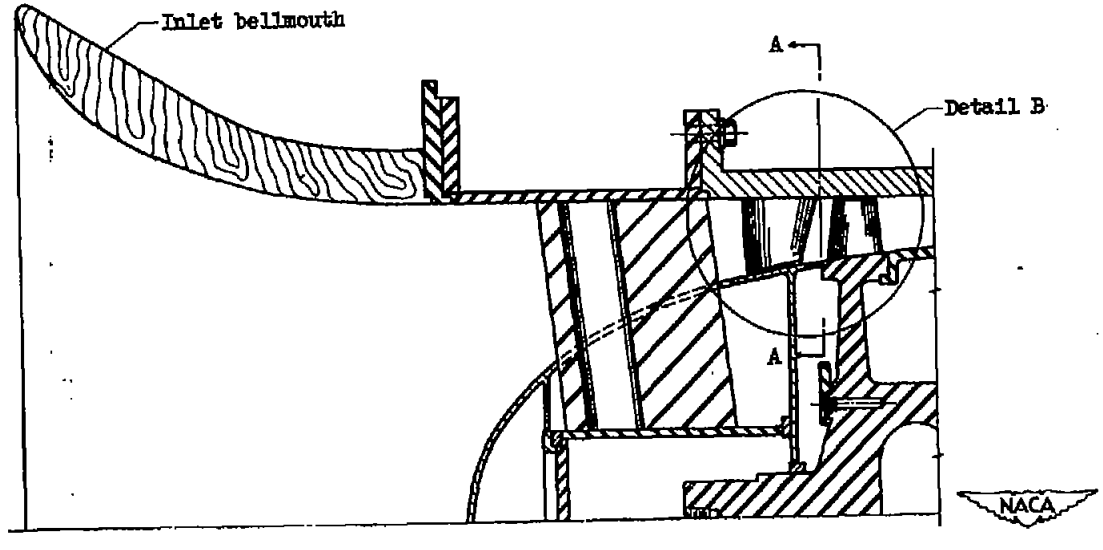

Figure 2. - Cross-sectional view of compressor showing instrument locations.

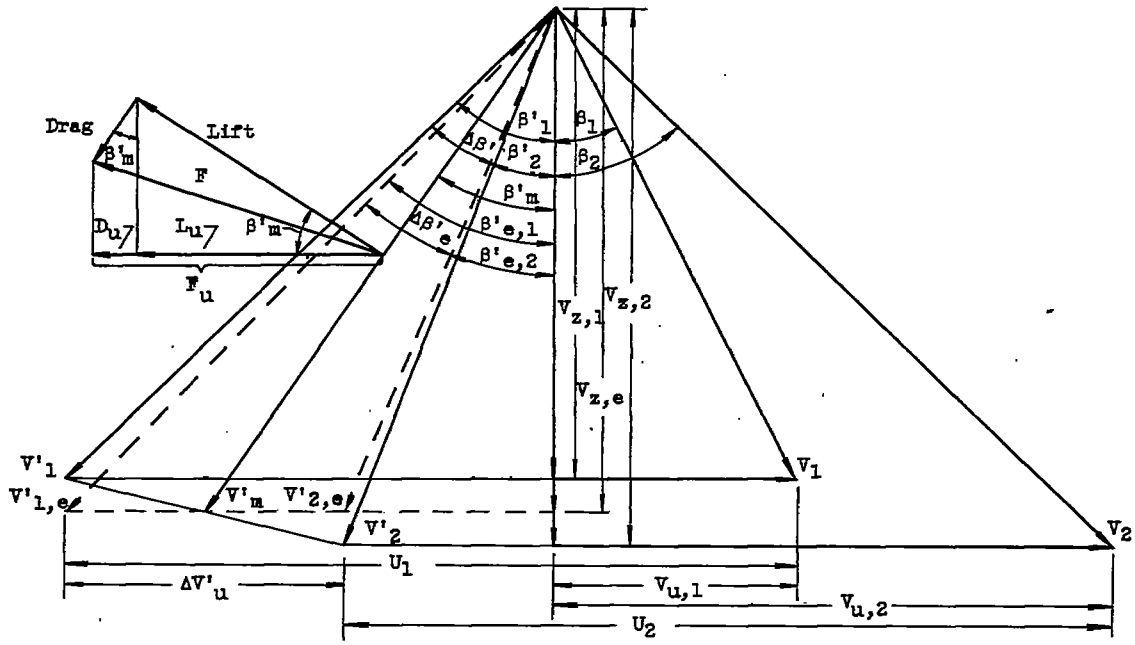

Figure 3. - Typical force diagram and variable axial-velocity diagram with equivalent values shown as dotted lines.

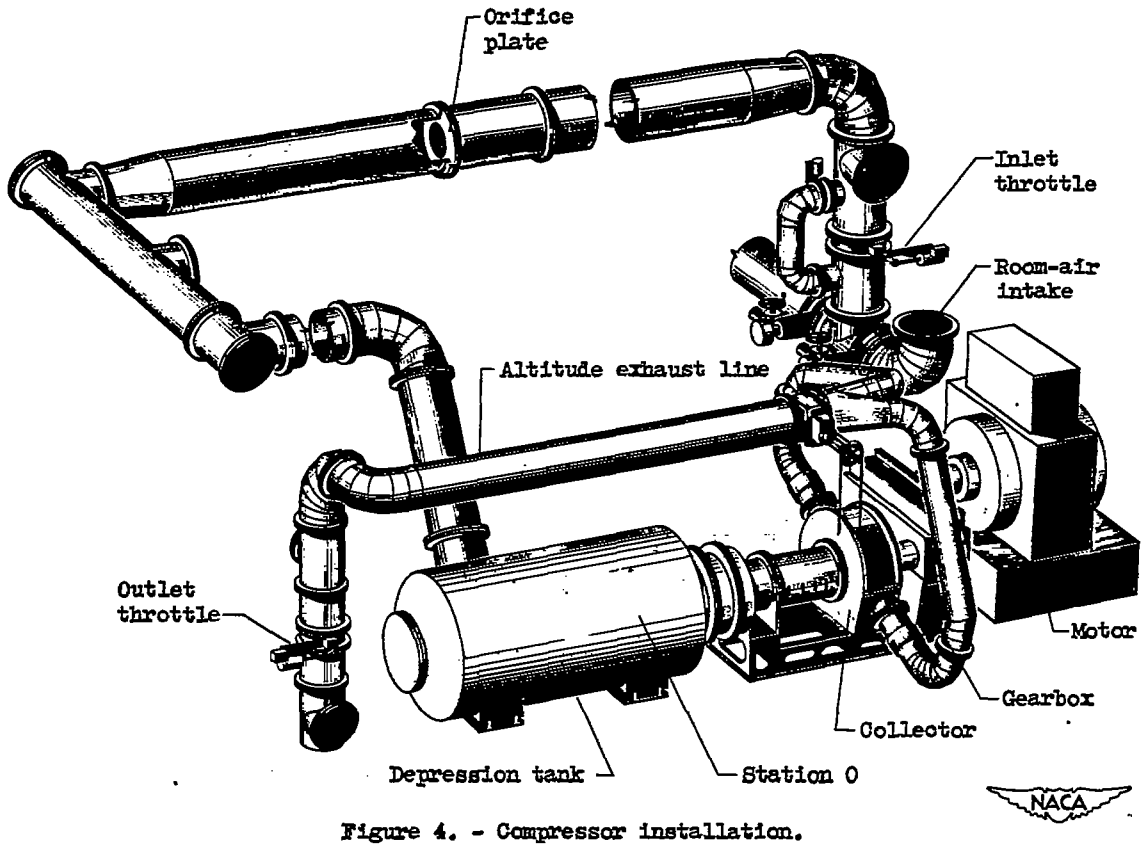

Figure 4. - Compressor installation.

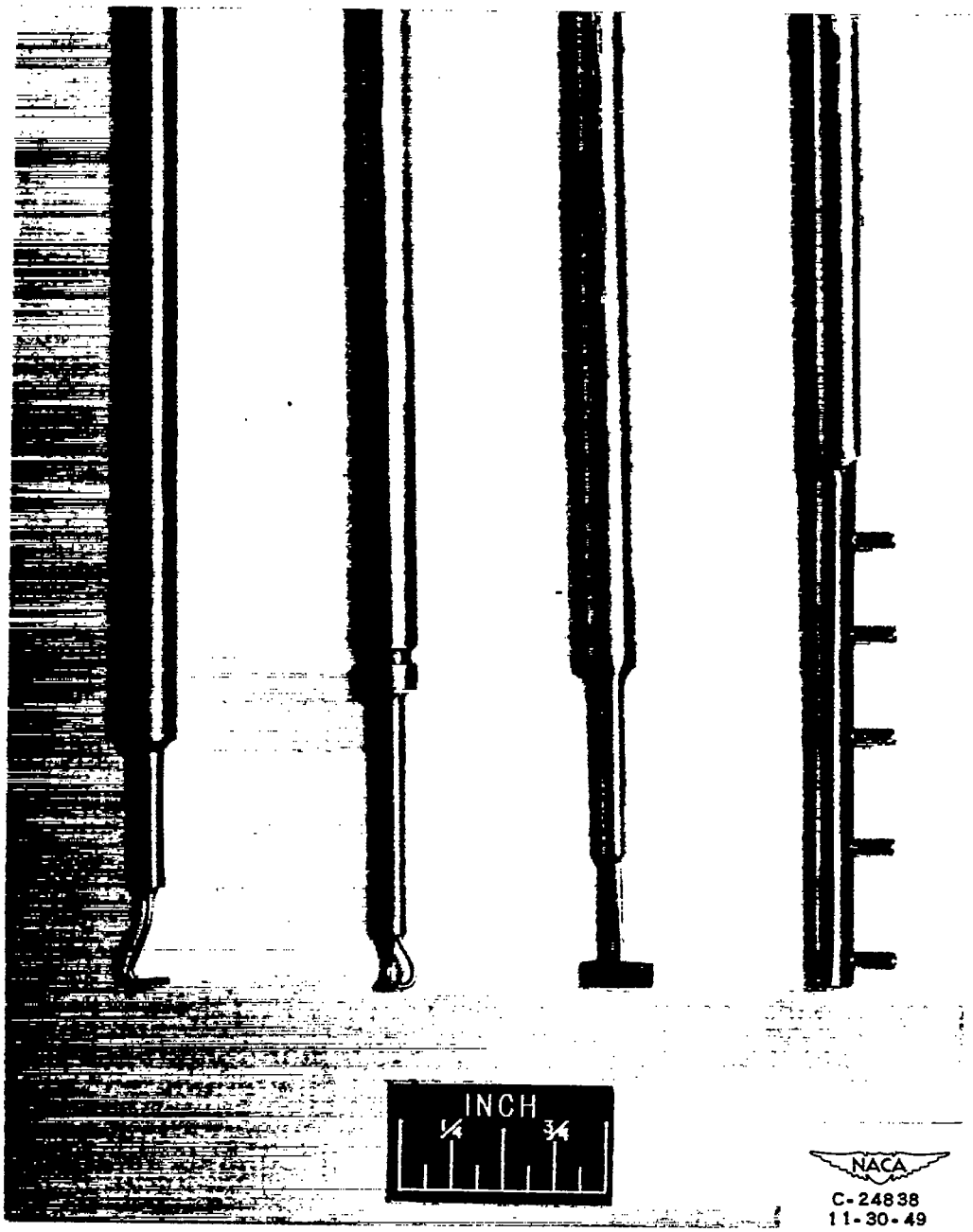

(a) Total-pressure survey probe. (b) Claw-type yaw tube. (c) Wedge-type static-pressure survey probe. (d) Thermocouple rake.

Figure 5. - Instruments.

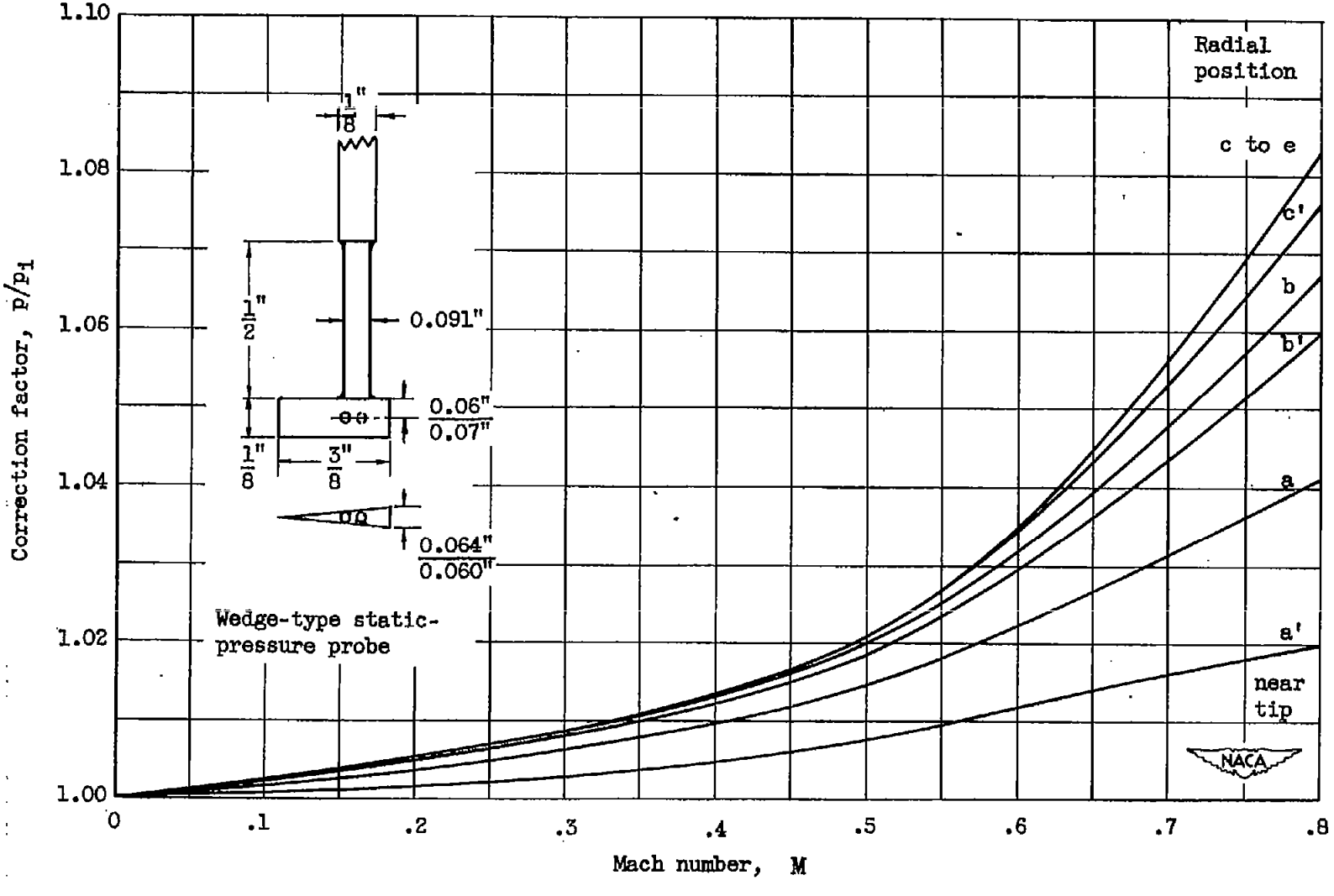

Figure 6. - Variation of wedge-type static-pressure-probe correction factor with Mach number for immersion distances corresponding to radial-survey positions investigated.

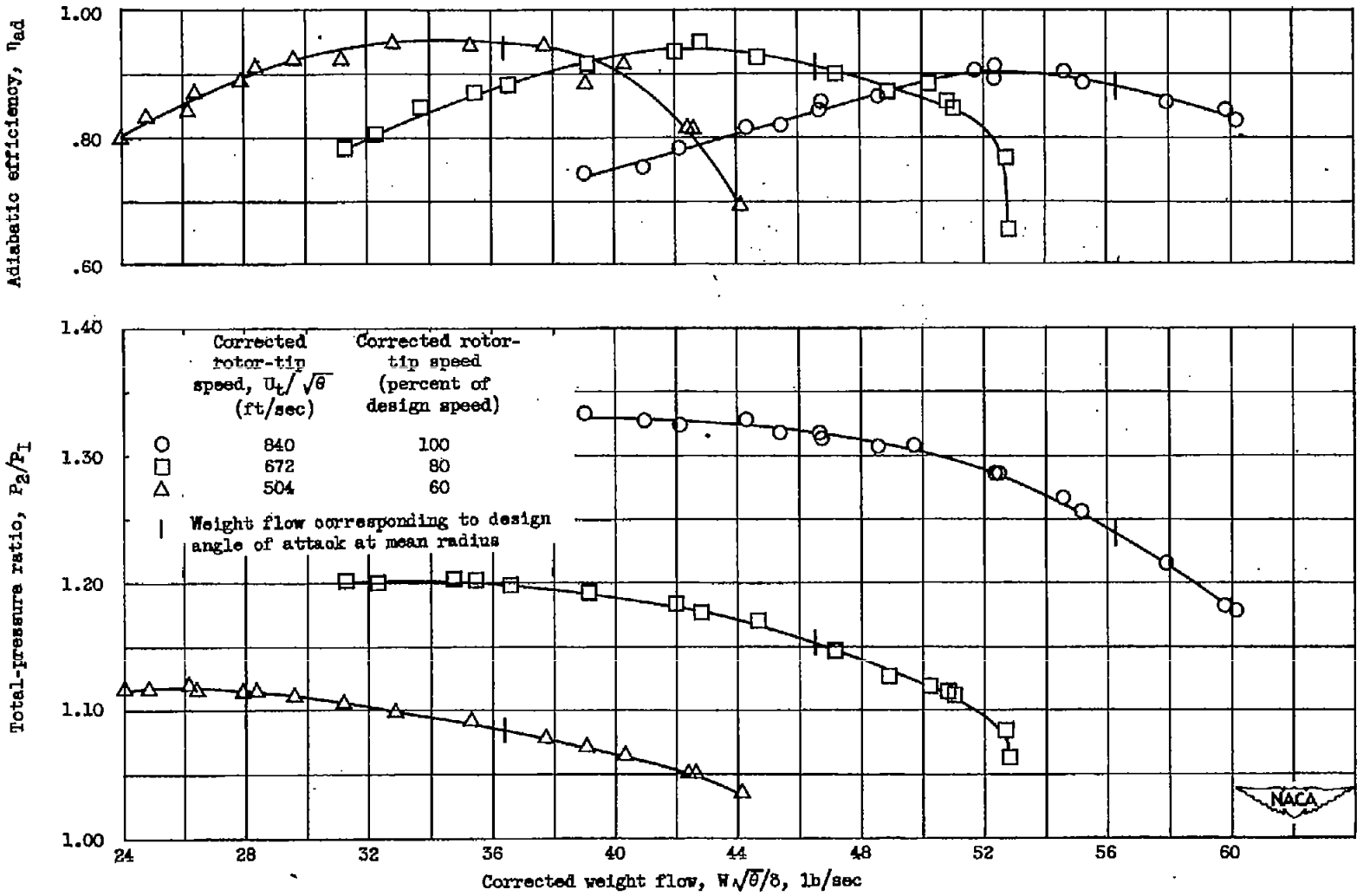

Figure 7. - Variation of total-pressure ratio and adiabatic efficiency across rotor with corrected weight flow at three rotor-tip speeds.

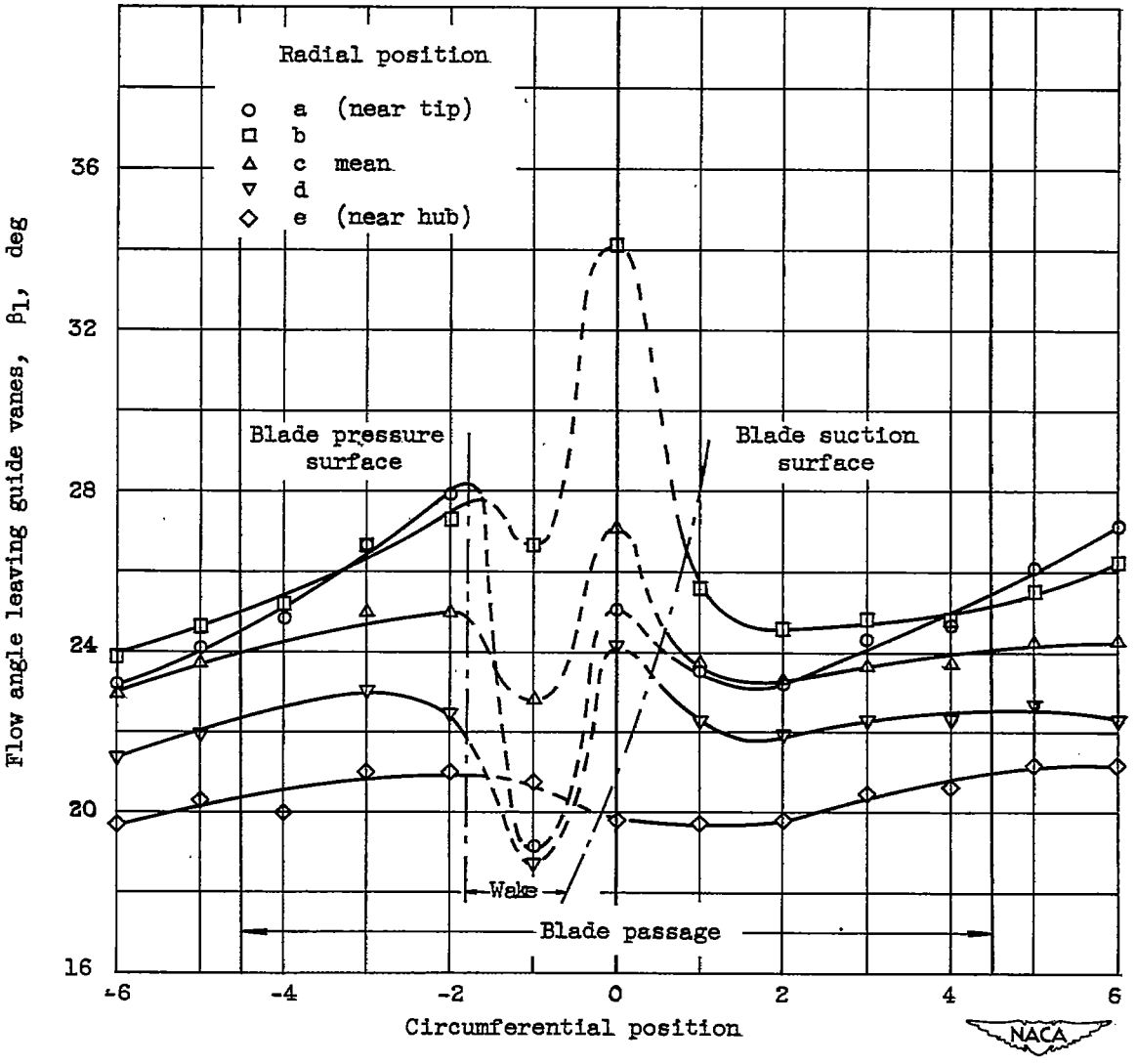

Figure 8. - Variation of flow angle with circumferential position downstream of guide vanes.

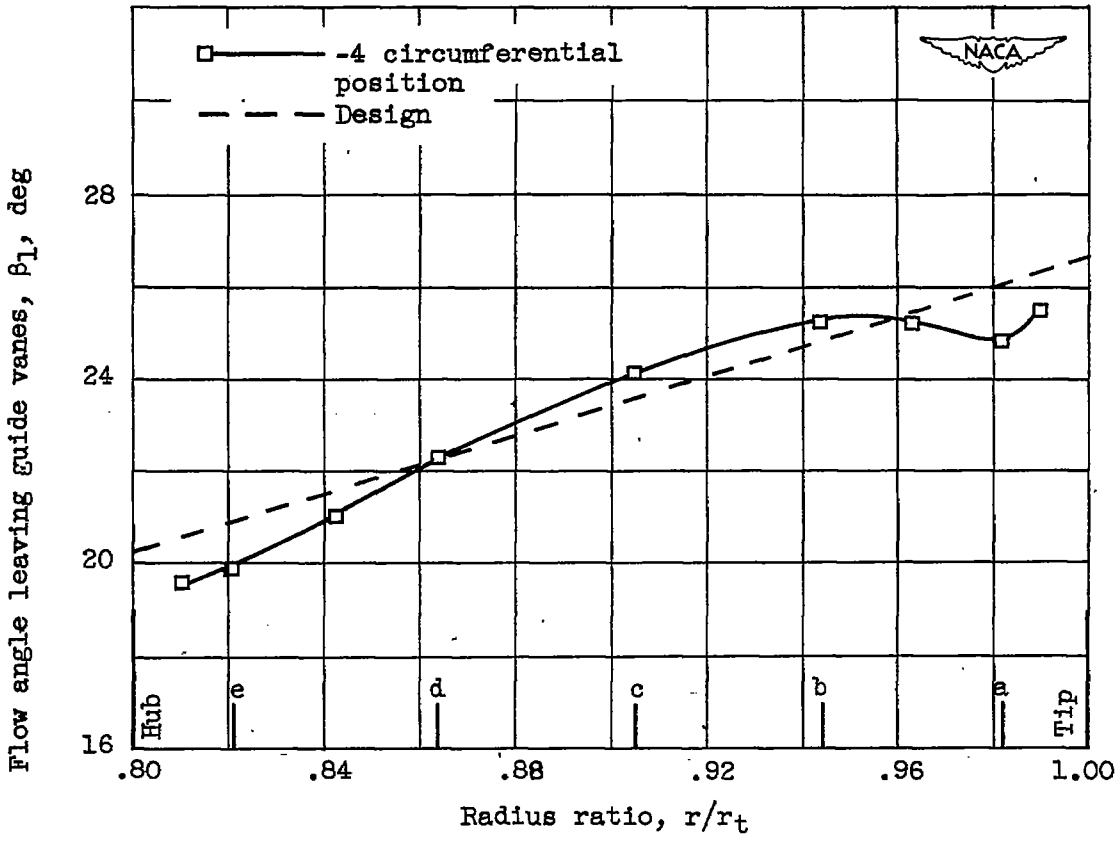

Figure 9. - Radial variation of flow angle leaving guide vanes without rotor.

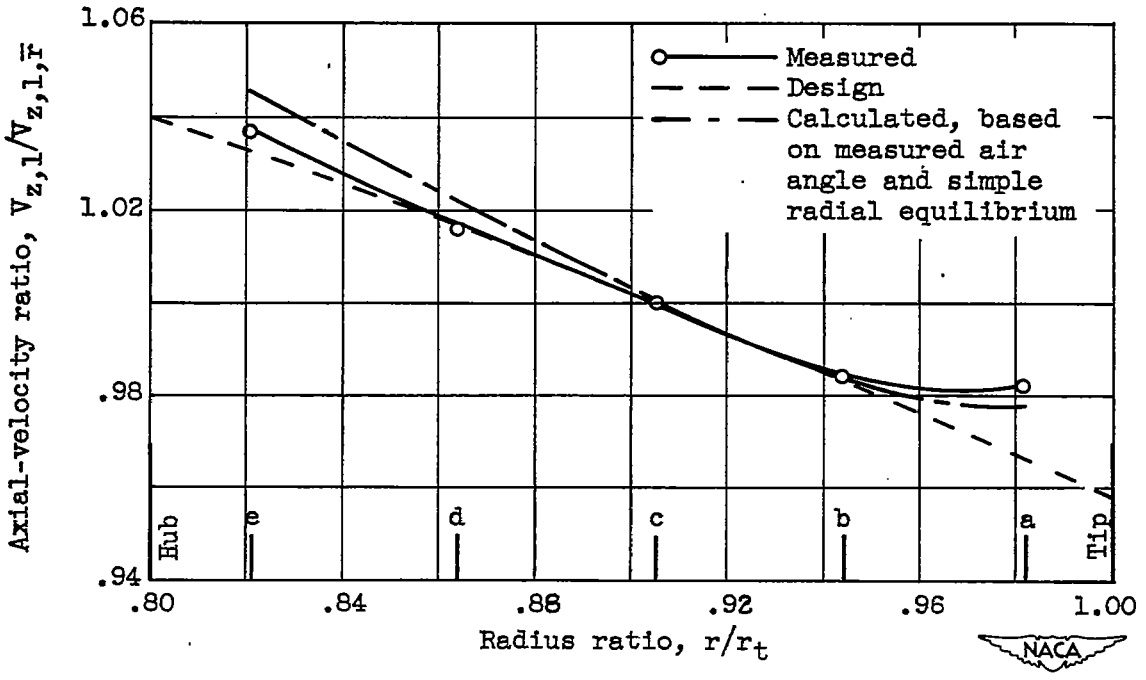

Figure 10. - Axial-velocity distribution downstream of guide vanes without rotor.

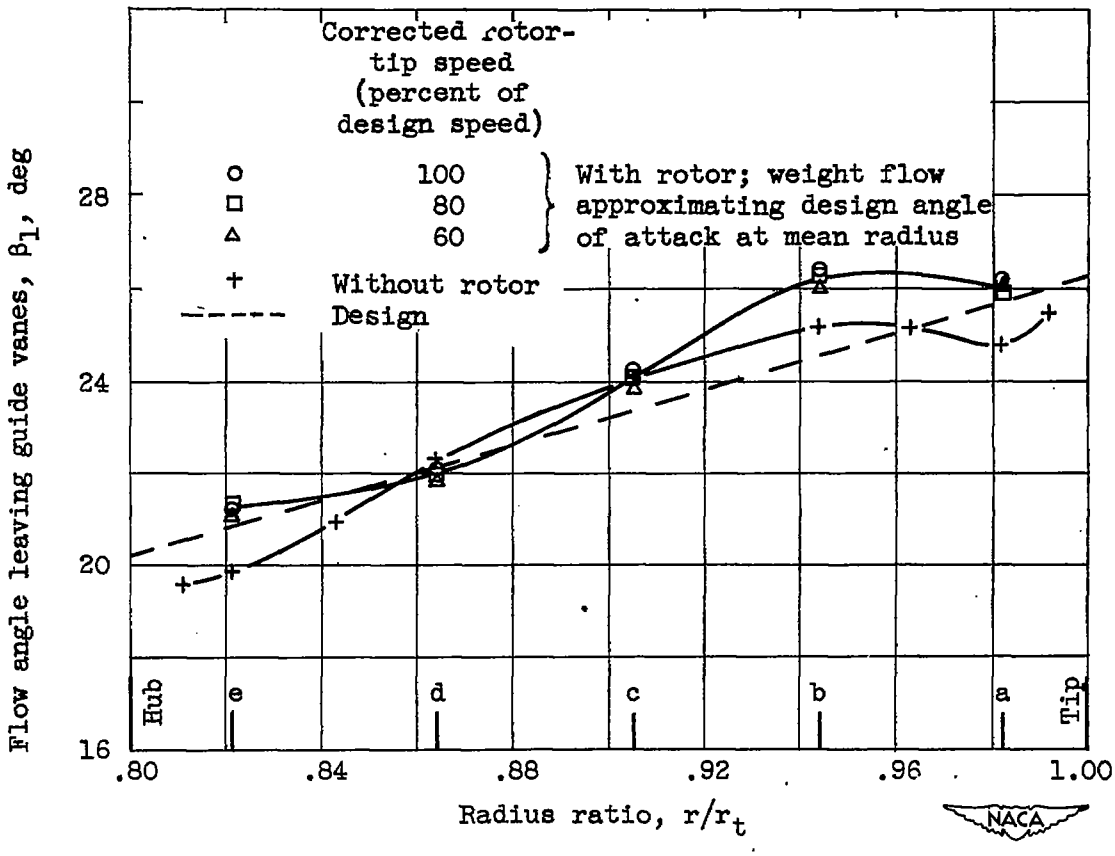

Figure 11. - Radial variation of flow angle leaving guide vanes at 60-, 80-, and 100-percent design speed corrected to guide-vane-inlet Mach number of 0.29 corresponding to investigation of guide vanes without rotor.

Figure 12. - Variation of flow angle leaving guide vanes with corrected weight flow at mean radius for 60-, 80-, and 100-percent design speed.

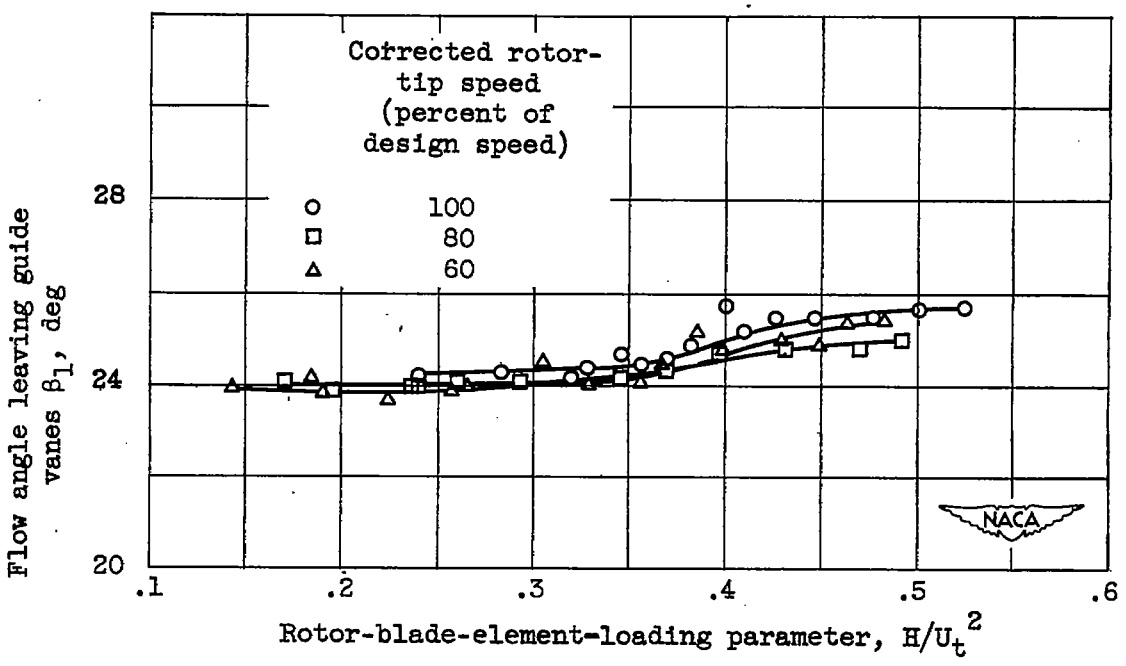

Figure 13. - Variation of flow angle leaving guide vanes at mean radius with dimensionless rotor-blade-element-loading parameter at 60-, 80-, and 100-percent design speed. Angles corrected to guide-vane-inlet Mach number of guide-vane investigations without rotor, according to reference 5.

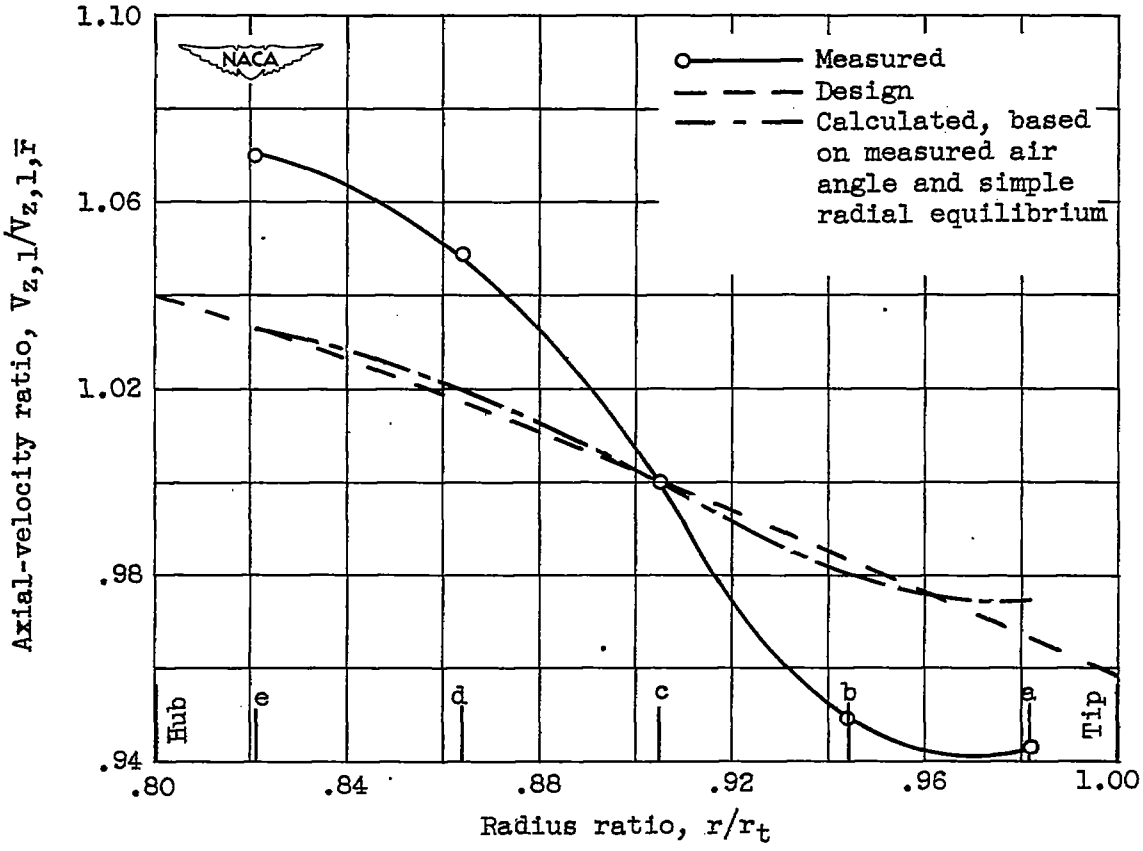

Figure 14. - Axial-velocity distribution downstream of guide vanes with rotor operating at design speed for a weight flow approximating design angle of attack at mean radius.

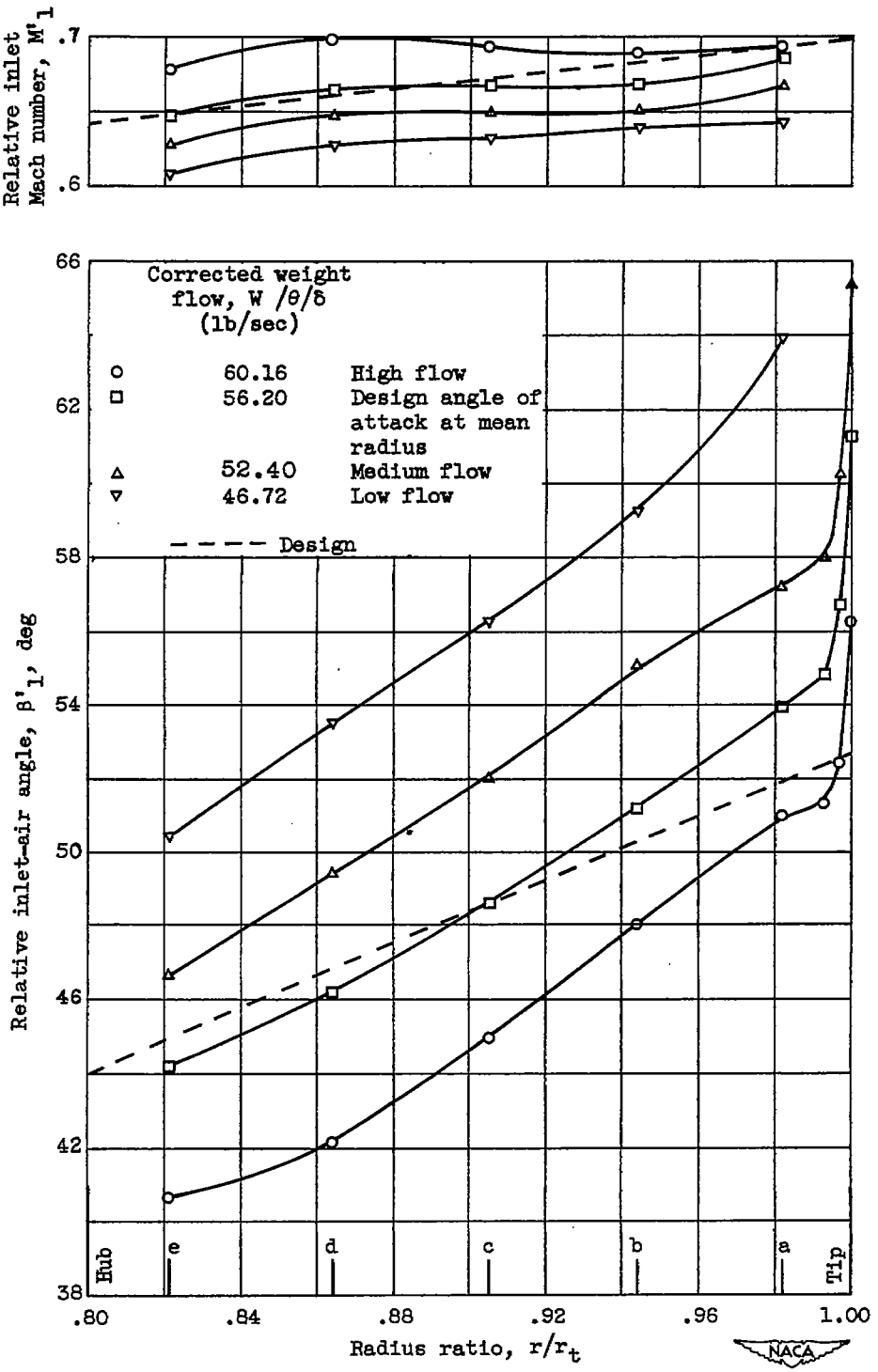

Figure 15. - Variation of relative inlet Mach number and relative inlet-air angle with radius ratio for four corrected weight flows at design speed.

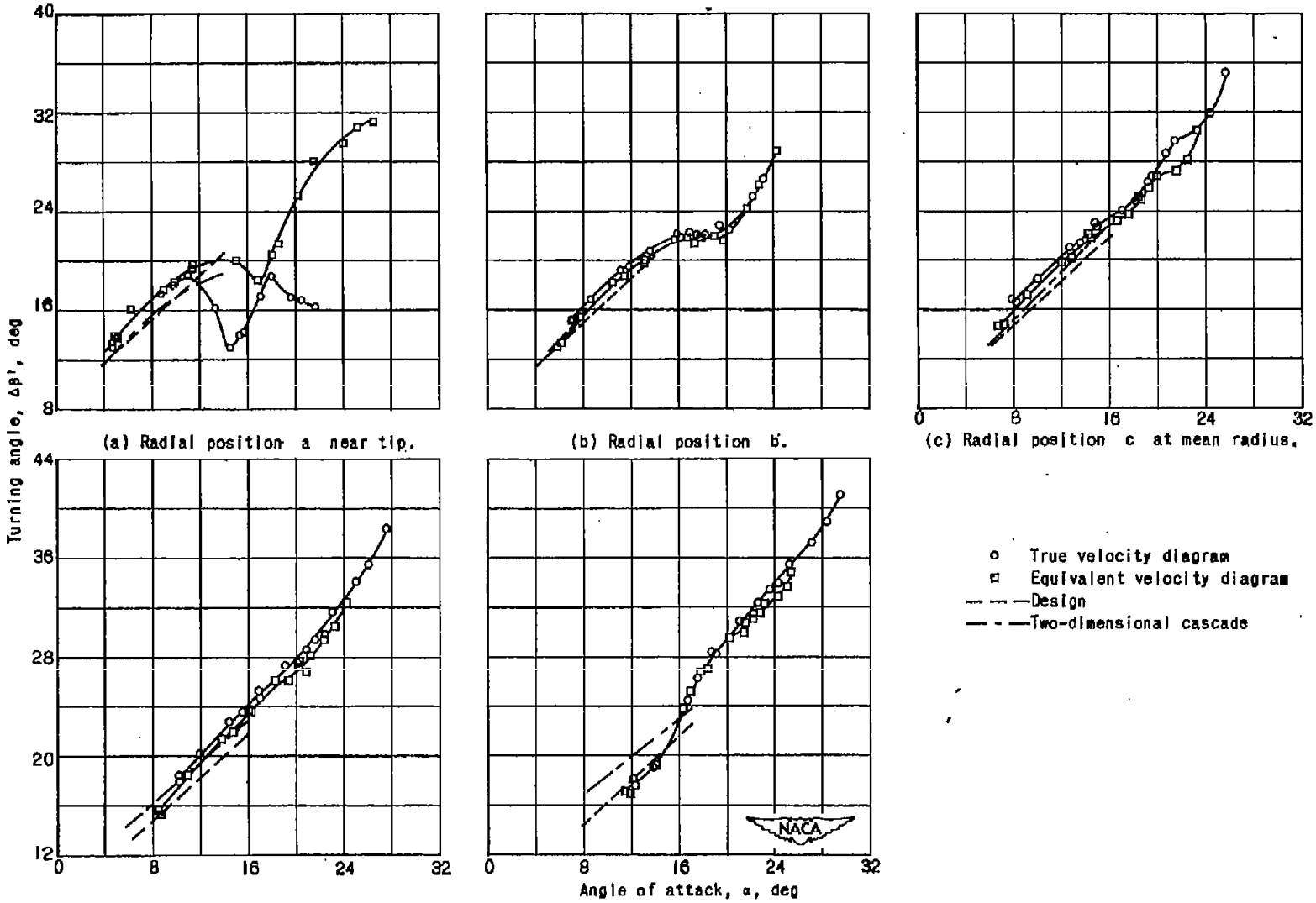

Figure 16. - Variation of turning angle across rotor blades with angle of attack at design speed.

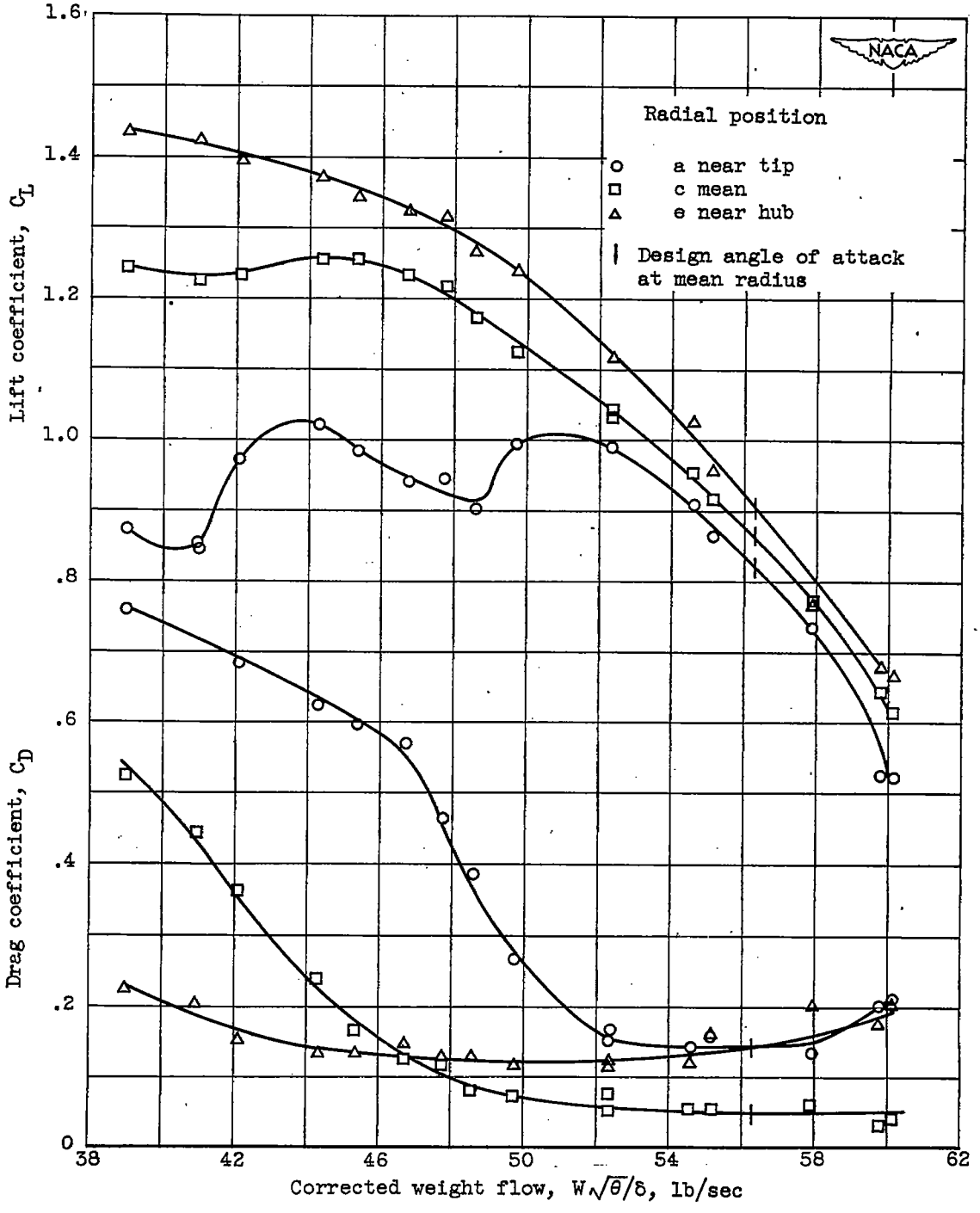

Figure 17. - Variation of lift and drag coefficient with corrected weight flow at tip, mean, and hub blade sections at design speed.

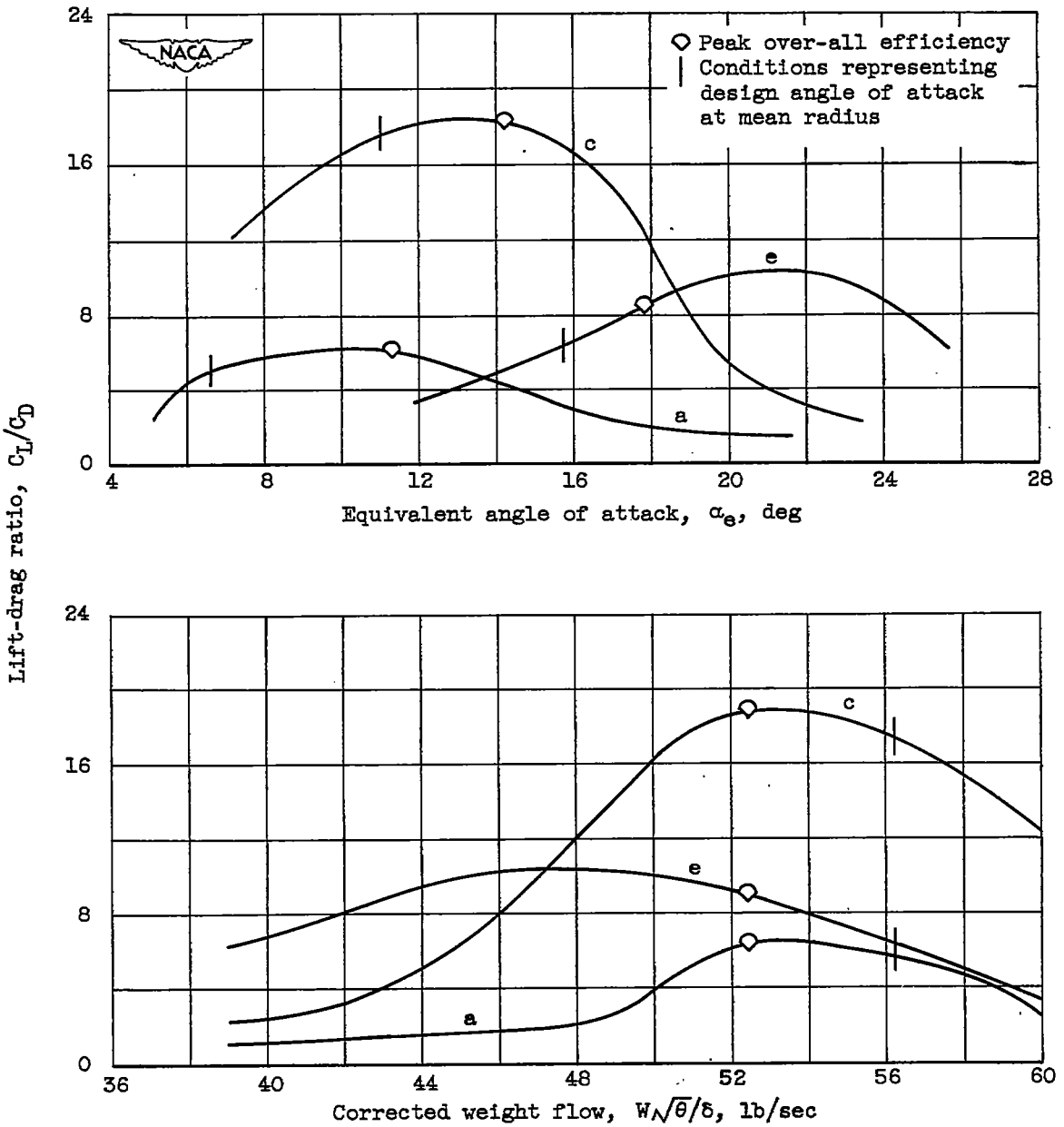

Figure 18. - Variation of rotor lift-drag ratio with corrected weight flow and equivalent angle of attack at tip, mean, and hub blade sections at design speed, as determined from faired curves of lift and drag coefficient in figure 17.

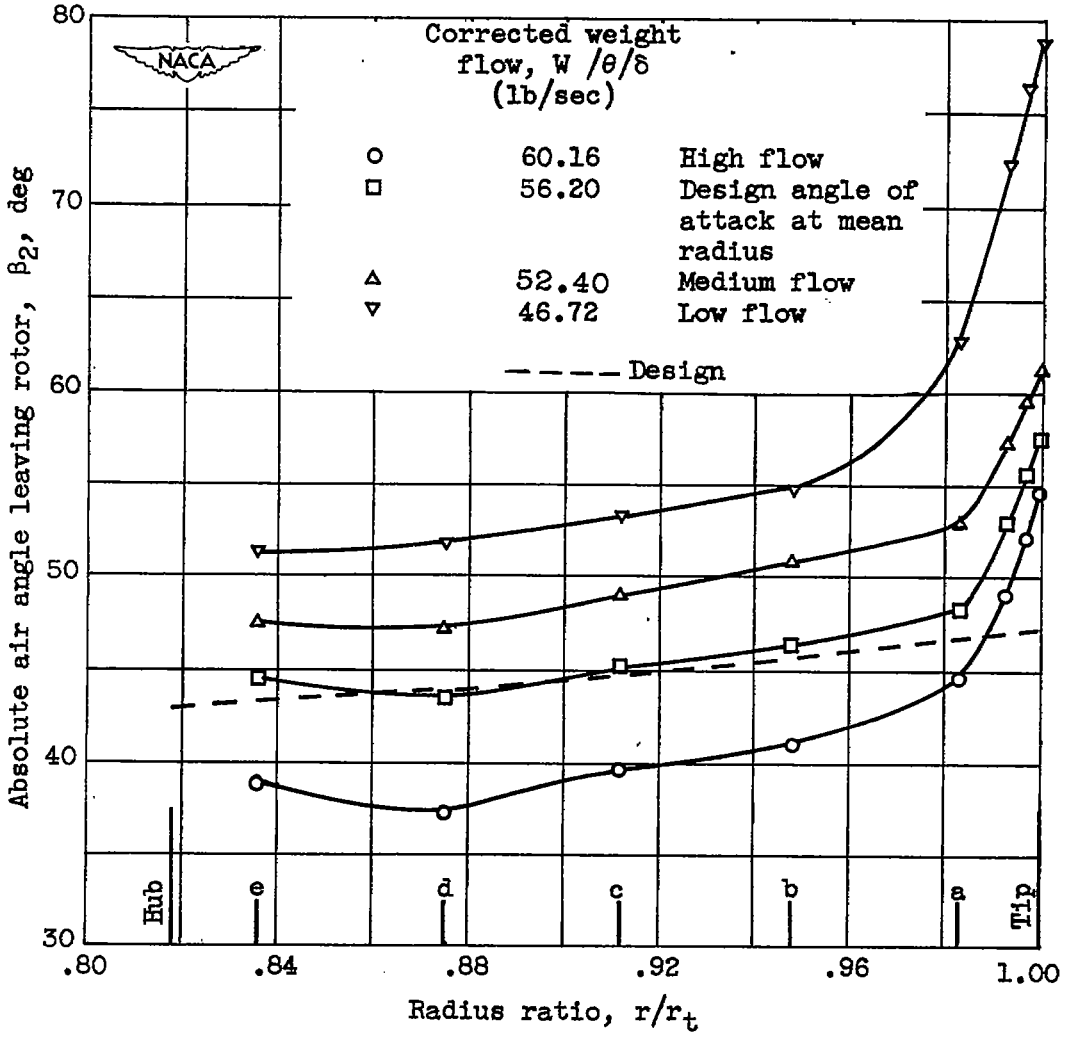

Figure 19. - Radial variation of absolute flow angle leaving rotor for four corrected weight flows at design speed.

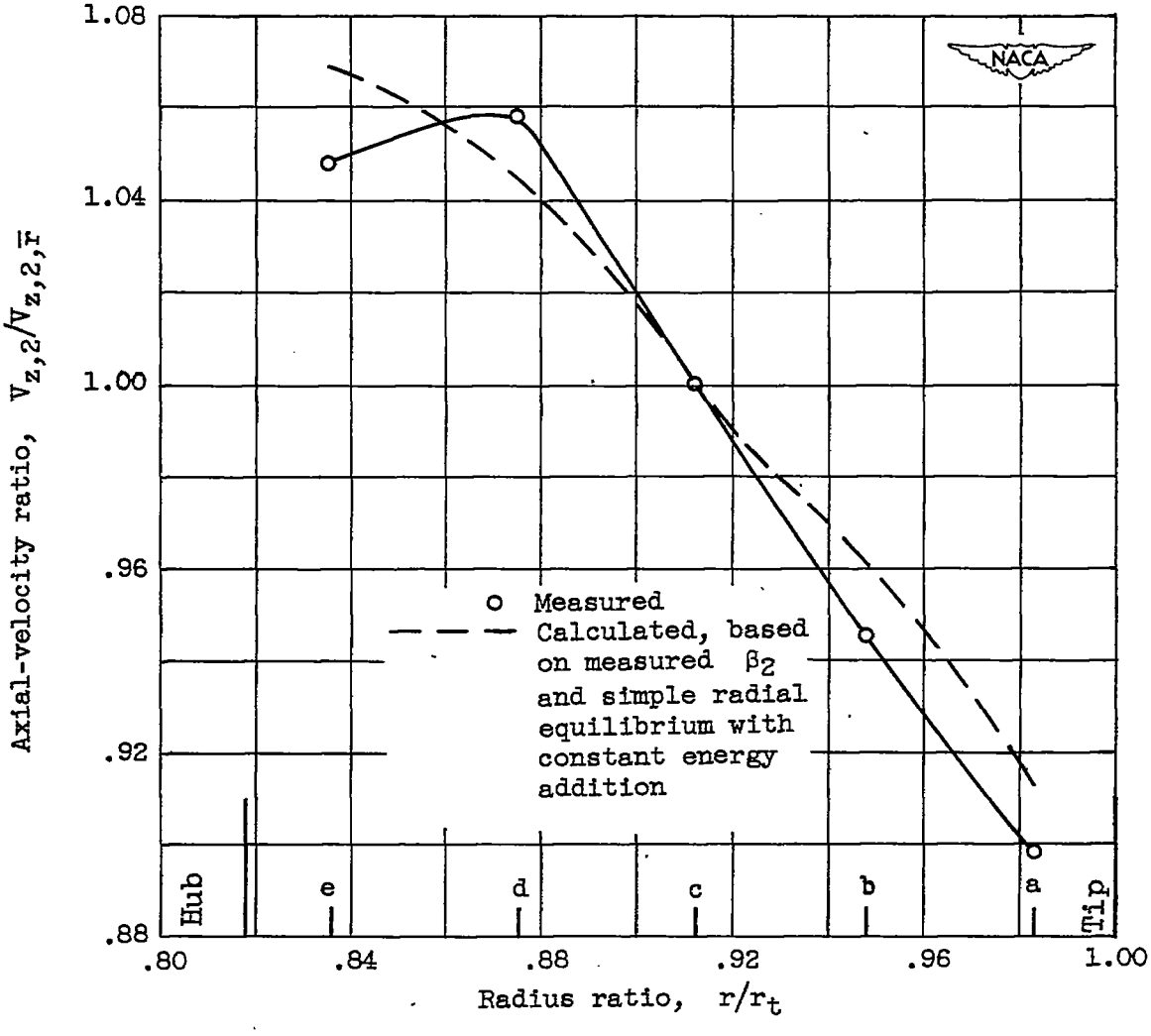

Figure 20. - Axial-velocity distribution downstream of rotor at design speed for approximately design angle of attack at mean radius.

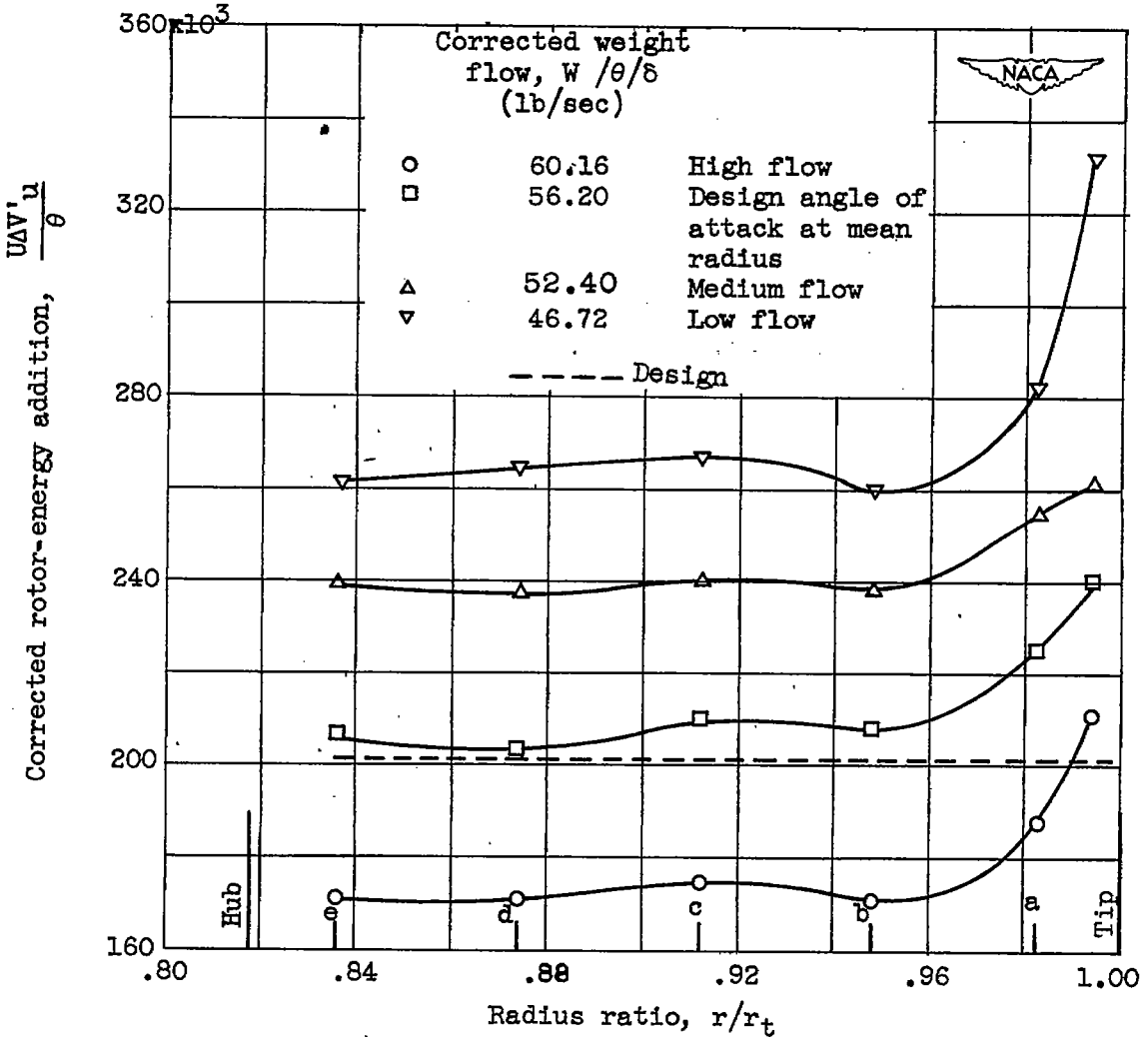

Figure 21. - Radial variation of corrected rotor energy addition for four corrected weight flows at design speed.

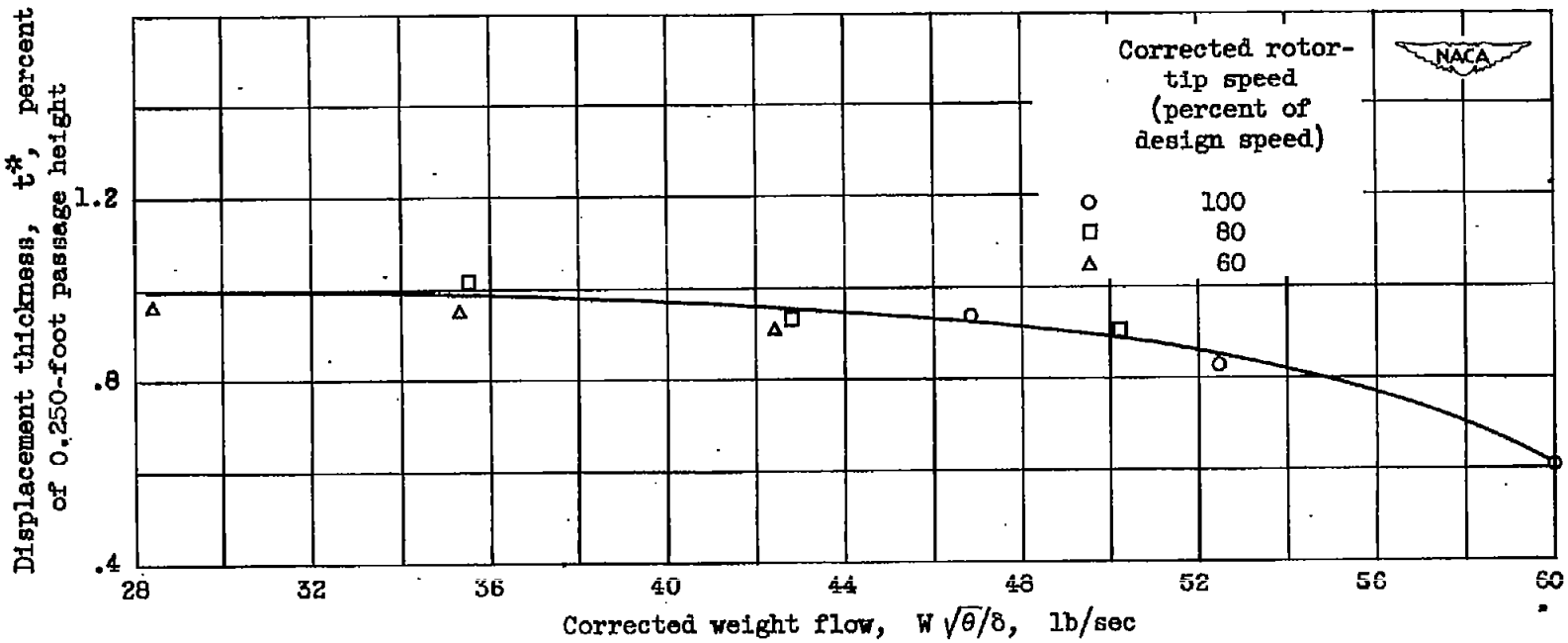

Figure 22. - Variation of outer wall boundary-layer displacement thickness downstream of guide vanes with corrected weight flow for three corrected tip speeds.

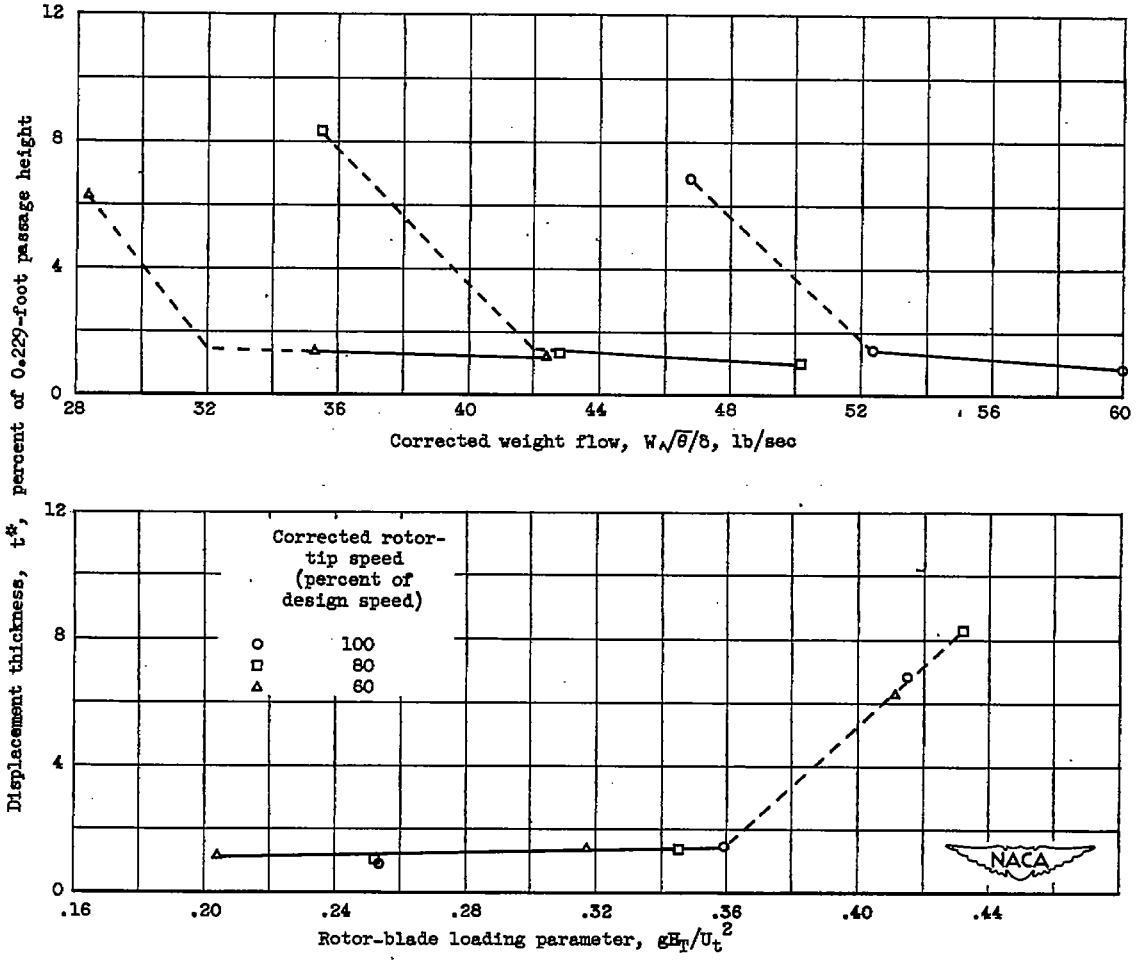

Figure 23. - Variation of outer-wall boundary-layer displacement thickness downstream of rotor with corrected weight flow and nondimensional rotor-blade loading parameter for three corrected tip speeds.